The Impact of Horizontal Resolution on North American Monsoon Gulf of California Moisture Surges in a Suite of Coupled Global Climate Models

SALVATORE PASCALE AND SIMONA BORDONI

California Institute of Technology, Pasadena, California

SARAH B. KAPNICK AND GABRIEL A. VECCHI

NOAA/Geophysical Fluid Dynamics Laboratory, Princeton, New Jersey

LIWEI JIA

Atmospheric and Oceanic Sciences Program, Princeton University, Princeton, New Jersey

THOMAS L. DELWORTH, SETH UNDERWOOD, AND WHIT ANDERSON

NOAA/Geophysical Fluid Dynamics Laboratory, Princeton, New Jersey

(Manuscript received 7 March 2016, in final form 28 July 2016)

ABSTRACT

The impact of atmosphere and ocean horizontal resolution on the climatology of North American monsoon Gulf of California (GoC) moisture surges is examined in a suite of global circulation models (CM2.1, FLOR, CM2.5, CM2.6, and HiFLOR) developed at the Geophysical Fluid Dynamics Laboratory (GFDL). These models feature essentially the same physical parameterizations but differ in horizontal resolution in either the atmosphere (≃200, 50, and 25 km) or the ocean (≃1°, 0.25°, and 0.1°). Increasing horizontal atmospheric resolution from 200 to 50 km results in a drastic improvement in the model's capability of accurately simulating surge events. The climatological near-surface flow and moisture and precipitation anomalies associated with GoC surges are overall satisfactorily simulated in all higher-resolution models. The number of surge events agrees well with reanalyses, but models tend to underestimate July–August surge-related precipitation and overestimate September surge-related rainfall in the southwestern United States. Large-scale controls supporting the development of GoC surges, such as tropical easterly waves (TEWs), tropical cyclones (TCs), and trans-Pacific Rossby wave trains (RWTs), are also well captured, although models tend to underestimate the TEW and TC magnitude and number. Near-surface GoC surge features and their large-scale forcings (TEWs, TCs, and RWTs) do not appear to be substantially affected by a finer representation of the GoC at higher ocean resolution. However, the substantial reduction of the eastern Pacific warm sea surface temperature bias through flux adjustment in the Forecast-Oriented Low Ocean Resolution (FLOR) model leads to an overall improvement of tropical–extratropical controls on GoC moisture surges and the seasonal cycle of precipitation in the southwestern United States.

1. Introduction

The North American monsoon (NAM) dominates the summertime seasonal cycle of rainfall over northwestern Mexico and the southwestern United States (Adams and Comrie 1997). Over most of this region, rainfall sharply increases in June, reaching its climatological maximum in August, and decreases again in September–October (Higgins et al. 1997). The NAM-related precipitation accounts for as much as approximately 70% of the total annual rainfall in the core monsoon region of northwestern Mexico and for approximately 40% to 50% in the southwestern United States (Douglas et al. 1993). Hence, the NAM significantly contributes to water resources in these areas with nonnegligible impacts on their economy, agriculture, and ecosystems.

Corresponding author address: Salvatore Pascale, California Institute of California, 1200 E. California Blvd., Pasadena, CA 91125.
E-mail: spascale@gps.caltech.edu

DOI: 10.1175/JCLI-D-16-0199.1

Over Arizona and western New Mexico (AZWNM), NAM rainfall is mainly associated with thunderstorms driven by daytime heating, with high-elevation terrains featuring an afternoon precipitation maximum and central Arizona lowlands featuring a near-midnight maximum (Balling 1987; King and Balling 1994). While modulated by daytime heating, AZWNM convective activity also features synoptic to submonthly variability (Berbery and Fox-Rabinovitz 2003; Wu et al. 2009; Pascale and Bordoni 2016), as revealed by significant spectral peaks in Arizona rainfall in the 5–20-day band or even longer time scales (e.g., Cavazos et al. 2002; Nolin and Hall-McKim 2006). Synoptic-scale convective activity over AZWNM tends to be preceded by Gulf of California (GoC) moisture surges (or simply GoC surges). These are coastally trapped, northward-propagating disturbances, characterized by anomalous southerly flow and moisture transport along the GoC (e.g., Hales 1972; Brenner 1974; Douglas et al. 1993; Adams and Comrie 1997; Stensrud et al. 1997; Bordoni et al. 2004; Zehnder 2004; Higgins et al. 2004; Rogers and Johnson 2007; Svoma 2010; Newman and Johnson 2012b, 2013). GoC surges modulate, and are responsible for, the establishment of the summertime GoC southerly low-level jet (Douglas 1995; Berbery 2001; Bordoni et al. 2004). While GoC surges are often initiated by outflows of mesoscale convective systems in the lower GoC region (Rogers and Johnson 2007; Mejia et al. 2010, 2015), associated precipitation over the southwestern United States is strongly linked to large-scale tropical and extratropical waves on synoptic (2–8 days; Stensrud et al. 1997; Higgins et al. 2004; Adams and Stensrud 2007; Ladwig and Stensrud 2009; Bieda et al. 2009; Bordoni and Stevens 2006; Schiffer and Nesbitt 2012; Seastrand et al. 2015), quasi-biweekly (10–20 days; Kiladis and Hall-McKim 2004; Jiang and Lau 2008; Kikuchi and Wang 2009), and subseasonal (25–90 days; Lorenz and Hartmann 2006; Jiang and Waliser 2009; Wu et al. 2009; Pascale and Bordoni 2016) time scales. In particular, Pascale and Bordoni (2016) show that strong precipitation events in this region are associated with time scales longer than synoptic, with the quasi-biweekly and subseasonal modes playing a dominant role in the occurrence of these more intense precipitative events. Thus, capturing GoC surge events, as well as their mesoscale and large-scale tropical and extratropical controls, appears to be essential to have some success in modeling the NAM precipitation.

Given the complex topographical features of the GoC region, modeling studies of GoC surges have so far been performed with regional climate models (RCMs; Anderson et al. 2000; Small 2001; Castro et al. 2007a,b; Newman and Johnson 2012b, 2013) or, less frequently, variable-resolution coupled general circulation models (GCMs) (e.g., Berbery and Fox-Rabinovitz 2003). While RCMs resolve finer-scale regional circulation features, they do not necessarily lead to improved simulations of regional climate because their output critically depends on the quality of the large-scale boundary conditions they are supplied with (Stratton 1999; Hay et al. 2006; Feser et al. 2011; Castro et al. 2007b, 2012). For example, comparing NAM simulations obtained from a coarse-resolution ($\simeq$200 km) version of the NCEP Global Forecast System with those from the NCEP 80-km RCM nested in it, Mo et al. (2005) concluded that the RCM is not able to overcome large-scale circulation deficiencies of the coarse-resolution model. Furthermore, the lack of an interactive coupling with their GCMs limits the reliability of RCM simulations, as it has been shown that a two-way coupling between the regional and planetary scales has a large impact on the large-scale circulation features of the GCM (Lorenz and Jacob 2005).

Simulations of the NAM rainfall, generally affected by dry biases over the southwestern United States, benefit from higher horizontal resolution as this allows them to better resolve the GoC and the associated northward moisture transport (e.g., Collier and Zhang 2007). Mo et al. (2005) show that some features of the GoC low-level jet emerge when increasing the horizontal resolution in a uniform-resolution GCM (NCEP Global Forecast System) from 200 to 80 km. The specific role of GoC surges in the GoC low-level jet and of the associated moisture transport in the monsoon precipitation is not, however, explored in Mo et al.'s (2005) study. State-of-the-art GCMs [e.g., those used to produce the archives of phases 3 and 5 of the Coupled Model Intercomparison Project (CMIP3 and CMIP5); Meehl et al. 2007; Taylor et al. 2013] still feature an atmospheric grid spacing that is too coarse ($\gtrsim$100 km) to adequately resolve the GoC. This significant limitation has so far prevented the analysis of GoC surges in studies on the NAM in the CMIP3 and CMIP5 GCMs (e.g., Liang et al. 2008; Geil et al. 2013).

Latest-generation GCMs developed at the Geophysical Fluid Dynamics Laboratory (GFDL) from CM2.1 (with an atmospheric resolution of approximately 200 km; Delworth et al. 2006) feature an atmosphere–land horizontal grid spacing of approximately 50 (Delworth et al. 2012; Vecchi et al. 2014) or 25 km (Murakami et al. 2015) and an oceanic horizontal resolution up to 0.1° (Table 1), which is higher than any current CMIP5 model resolution and comparable to that of RCMs. The increased resolution allows these models to simulate successfully detailed features of some regional hydroclimates (e.g., Kapnick and Delworth 2013; Delworth and Zeng 2014; Kapnick et al. 2014; Jia et al. 2015).

TABLE 1. Summary of the six GFDL models used in this study. Values reported for atmosphere and ocean horizontal resolution are approximate (lat × lon; more details in the references).

Model	Atmosphere resolution (horizontal/vertical layers)	Ocean resolution (horizontal/vertical layers)	General reference
CM2.1	2° × 2°/L24	1° × 1°/L50	Delworth et al. (2006)
FLOR	0.5° × 0.5°/L32	1° × 1°/L50	Vecchi et al. (2014)
FLOR-FA	0.5° × 0.5°/L32	1° × 1°/L50	Vecchi et al. (2014)
HiFLOR	0.25° × 0.25°/L32	1° × 1°/L50	Murakami et al. (2015)
CM2.5	0.5° × 0.5°/L32	0.25° × 0.25°/L50	Delworth et al. (2012)
CM2.6	0.5° × 0.5°/L32	0.1° × 0.1°/L50	Delworth et al. (2012)

The peculiar shape and placement of the GoC is crucial for the NAM to be able to extend into AZWNM, as it allows for lower-level moist tropical air masses to be channeled northward into the northern monsoon region (e.g., Hu and Dominguez 2015). As a consequence, we expect GoC surges to be progressively better simulated when going from lowest- to highest-resolution model. More specifically, here we ask the following:

- Does the representation of GoC surges and their main features improve as the atmosphere and ocean horizontal resolution increases in a fully coupled GCM?
- Are the large-scale controls of GoC surges, such as midlatitude Rossby waves and tropical easterly waves, less sensitive to model resolution than smaller-scale circulations? That is to say, is it reasonable to expect that they will be adequately captured even by lower-resolution models?

To answer these questions, we will assess how five GFDL GCMs with different horizontal resolutions but essentially identical physical parameterizations simulate 1) GoC surge frequency (number of surges per summer), 2) their contribution to the monsoon precipitation, 3) their dynamical and thermodynamical structure, and 4) their relationship to large-scale tropical and extratropical waves. In addition to the questions stated above, the availability of a flux-adjusted simulation for one of these models [the Forecast-Oriented Low Ocean Resolution (FLOR) model; Table 1] allows for an evaluation of the influence of its Pacific Ocean sea surface temperature (SST) biases on GoC surges and their dynamical controls. As the atmosphere can respond to SST anomalies with Rossby waves (e.g., Ferreira and Frankignoul 2005), we expect that the most notable differences will be in the large-scale controls of the GoC surges rather than in their near-surface features.

This is the first study to provide a detailed analysis of GoC surges in global coupled GCMs of uniform horizontal resolution. Given the large uncertainty of GCM projections of the NAM response in the southwestern United States (e.g., Cook and Seager 2013; Pascale et al. 2016), assessing the simulated present-day synoptic-scale variability, such as that associated with GoC surges, is a necessary effort to gain any mechanistic understanding of how the NAM will respond to global warming or to build a basis for dynamical seasonal prediction of the NAM. The paper will be structured as follows. In section 2, we give a brief overview of the GFDL models and other datasets used in this study and describe our methodology to evaluate GoC surges. In section 3, we assess how well these models simulate GoC surges in terms of their lower-level flow and associated moisture flux, their influence on the NAM precipitation, and their larger-scale controls. In section 4, we investigate the relationship between tropical and extratropical waves and GoC surges both in reanalysis and models. A critical discussion is provided in section 5, and a summary follows in section 6.

2. Data and methods

Below, we provide a description of the GFDL models, observational products, and the overall methodology employed in this study.

a. Models

The following coupled models are considered here (see Table 1):

- GFDL Coupled Model version 2.1 (CM2.1) features a horizontal grid spacing of 2° for the atmosphere and land components and of 1° for the ocean and sea ice components. CM2.1 was included in the CMIP3 and CMIP5 archives and has been extensively analyzed for the Fourth Assessment Report (AR4) of the Intergovernmental Panel on Climate Change (IPCC) and used for predictability and seasonal-to-decadal variability research (e.g., Wittenberg et al. 2006; Vecchi et al. 2013; Yang et al. 2013; Wittenberg et al. 2014). A detailed description of CM2.1 is found in Anderson et al. (2004) and Delworth et al. (2006).
- GFDL Coupled Model version 2.5 (CM2.5) has a horizontal resolution of approximately 50 km for the atmosphere and 0.25° for the ocean (from 28 km at the equator to 8 km at high latitudes). Except for some minor changes in the cloud scheme and a much improved land model (Milly et al. 2014), the atmospheric

physics parameterizations are almost identical to those of CM2.1. More details about CM2.5 are in Delworth et al. (2012). CM2.5 has been used to understand climate extremes (e.g., Kim et al. 2014; Delworth et al. 2015) and ocean circulations (Lee et al. 2013). Thanks to its increased horizontal resolution, CM2.5 has proven very effective for studying regional hydroclimatic change (Kapnick and Delworth 2013; Delworth and Zeng 2014; Kapnick et al. 2014).

- GFDL Coupled Model version 2.6 (CM2.6) has the same atmosphere–land component as CM2.5, also including ocean and sea ice physics, but has a substantially higher horizontal resolution for the ocean component (grid spacing varying from 11 km at the equator to roughly 4 km near the poles). This results in a much more realistic simulation of mesoscale eddy activity in the ocean (Delworth et al. 2012).
- The FLOR model, a version of CM2.5, has an atmosphere–land model as in CM2.5 but with a lower horizontal resolution (1° vs 0.25°) for the ocean–sea ice components (Vecchi et al. 2014). The lower ocean-sea ice resolution reduces considerably computational times if compared to CM2.5, allowing for large ensembles of simulations while preserving almost all of the improvements seen in CM2.5 with respect to CM2.1 (e.g., Jia et al. 2015). In addition to the standard version of FLOR, we also use the flux-adjusted version of FLOR (FLOR-FA), where climatological adjustments are made to FLOR surface fluxes of momentum, enthalpy, and freshwater in order to bring the model climatology of surface wind stress and SST closer to the observed 1979–2012 climatology. Please refer to Vecchi et al. (2014) for further details about the method used for the flux adjustment.
- The High-Resolution Forecast-Oriented Low Ocean Resolution (HiFLOR) model is identical to FLOR but has a halved grid spacing for the atmospheric model (≃25 km) and most of the subgrid-scale physical parameterizations unchanged relative to FLOR. As a result, HiFLOR has a better representation, compared to FLOR, of extreme events such as category 4 and 5 hurricanes (Murakami et al. 2015) and precipitation extremes (van der Wiel et al. 2016).

The main parameterizations used in the atmosphere and land model of these GCMs are summarized in Table 2.

For all models, we use a 100-yr control run with atmospheric composition (greenhouse gases and aerosols) and external forcing (solar irradiance) fixed at 1990 levels. These models allow for a systematic exploration of the effect of horizontal resolution on GoC surges. In particular, CM2.1, FLOR, and HiFLOR all share the same ocean–sea ice model with 1° horizontal grid spacing but have an increasing horizontal resolution in their atmospheric component (200, 50, and 25 km, respectively) and thus an increasing realism in the representation of topographical features (Fig. 1). FLOR, CM2.5, and CM2.6 instead have the same atmospheric component with 50-km horizontal grid spacing but increasing ocean horizontal resolution of 1°, 0.25°, and 0.1°, respectively (Table 1). The land–sea distribution of the GoC region therefore varies from being completely unresolved in CM2.1 to being fairly realistic in CM2.5 and CM2.6 (Fig. 2). FLOR has a realistic representation of the GoC topography but, owing to lower ocean resolution, an only partially resolved GoC, with land rather than seawater north of 27°N. Furthermore, FLOR-FA allows for an assessment of the influence on GoC surges of the biases in the long-term SST climatology, in particular over the Gulf of Mexico and the eastern Pacific (Vecchi et al. 2014). Model details are summarized in Table 1.

b. Observations

Model performances are assessed against observations provided by the European Centre for Medium-Range Weather Forecasts interim reanalysis (ERA-Interim, herein ERA-I) product (Dee et al. 2011; Berrisford et al. 2011a), available for the period 1979–2014. The ERA-I atmospheric model has 60 vertical levels and a horizontal resolution of about 79 km (Berrisford et al. 2011b), which is sufficient to resolve the GoC and the topographical features of the region (Figs. 2a and 1a). In addition to ERA-I, we also use the National Aeronautics and Space Administration (NASA) Goddard Space Flight Center (GSFC) Modern-Era Retrospective Analysis for Research and Applications (MERRA, available for the period 1979–2010; Rienecker et al. 2011) for variables not readily available in ERA-I (e.g., near-surface specific humidity) and to verify consistency of results from the two different reanalyses. MERRA has vertical (72 levels) and horizontal resolutions (0.5° latitude × 0.67° longitude) that are comparable to those of ERA-I.

As in Pascale and Bordoni (2016), the focus of this study is on the influence of GoC surges on precipitation over AZWNM, defined as the area between 114° and 108°W and between 31° and 36°N (Fig. 1). We do not include eastern New Mexico because summertime rainfall in this region is mainly influenced by upslope winds from the Great Plains (Lorenz and Hartmann 2006). To have further confidence in the realism of the summertime precipitation over AZWNM, we also include in our analysis precipitation estimates from the Global Precipitation Climatology Centre (GPCC) dataset (Schneider et al. 2014; Becker et al. 2013). GPCC is based on statistically interpolated in situ rain measurements and covers all land areas at monthly temporal resolution for the period 1901–2010.

TABLE 2. Summary of the main different and common atmosphere and land parameterizations. All models have no aerosol or chemistry parameterization. Detailed descriptions of each scheme can be found in Anderson et al. (2004) and Delworth et al. (2012).

Component	Model	
	CM2.1	CM2.5, CM2.6, FLOR, and HiFLOR
Land model	Land Model 2 (LM2; Milly and Shmakin 2002). Isothermal surface (soil–snow–vegetation); three water stores: snow, root zone, and groundwater; soil temperature levels to 6-m total depth; stomatal control of evapotranspiration; latent heat storage in soil; and surface parameters dependent on eight soil and eight vegetation types.	Land Model 3 (LM3; Milly et al. 2014). Multilayer model of snowpack above the soil; continuous vertical representation of soil water; frozen soil-water phase; parameterization of water-table height, saturated-area fraction, and groundwater discharge to streams derived from standard groundwater–hydraulic assumptions and surface topographic information; finite-velocity horizontal transport of runoff via rivers to the ocean; and lakes, lake ice, and lake ice–snowpacks that exchange mass and energy with both the atmosphere and the rivers.
Dynamics	Hydrostatic, finite-difference dynamical core (Mesinger et al. 1988); staggered Arakawa B grid.	Hydrostatic, finite-difference dynamical core (Mesinger et al. 1988); ''cubed sphere'' grid (Putman and Lin 2007); spherical atmosphere is represented on six sides of a cube.
Longwave radiation	Simplified exchange approximation; H_2O continuum parameterization (Schwarzkopf and Ramaswamy 1999; Clough et al. 1992).	
Shortwave radiation	Exponential sum fit with 18 bands (Freidenreich and Ramaswamy 1999); liquid cloud radiative properties from Slingo (1989); and ice cloud radiative properties from Fu and Liou (1993).	
Clouds	Three prognostic tracers: cloud liquid, cloud ice, and cloud fraction; cloud microphysics scheme from Rotstayn (1997) and cloud macrophysics scheme from Tiedtke (1993).	
Convection	Relaxed Arakawa–Schubert scheme (Moorthi and Suarez 1992); convective momentum transport represented by vertical diffusion proportional to the cumulus mass flux.	
Vertical diffusion	Surface and stratocumulus convective layers represented by a K-profile scheme with prescribed entrainment rates (Lock 2001); surface fluxes from Monin–Obukhov similarity theory; gustiness enhancement to wind speed used in surface flux calculations (Beljaars 1995); enhanced near-surface mixing in stable conditions; and orographic roughness effects included.	
Gravity wave drag	Orographic drag scheme from Stern and Pierrehumbert (1988).	
Ocean mesoscale eddy	Parameterization for the effects of mesoscale eddies in CM2.1, FLOR, and HiFLOR (Griffies et al. 2005; Gnanadesikan et al. 2006); CM2.5 and CM2.6 have no eddy parameterization (eddy resolving).	

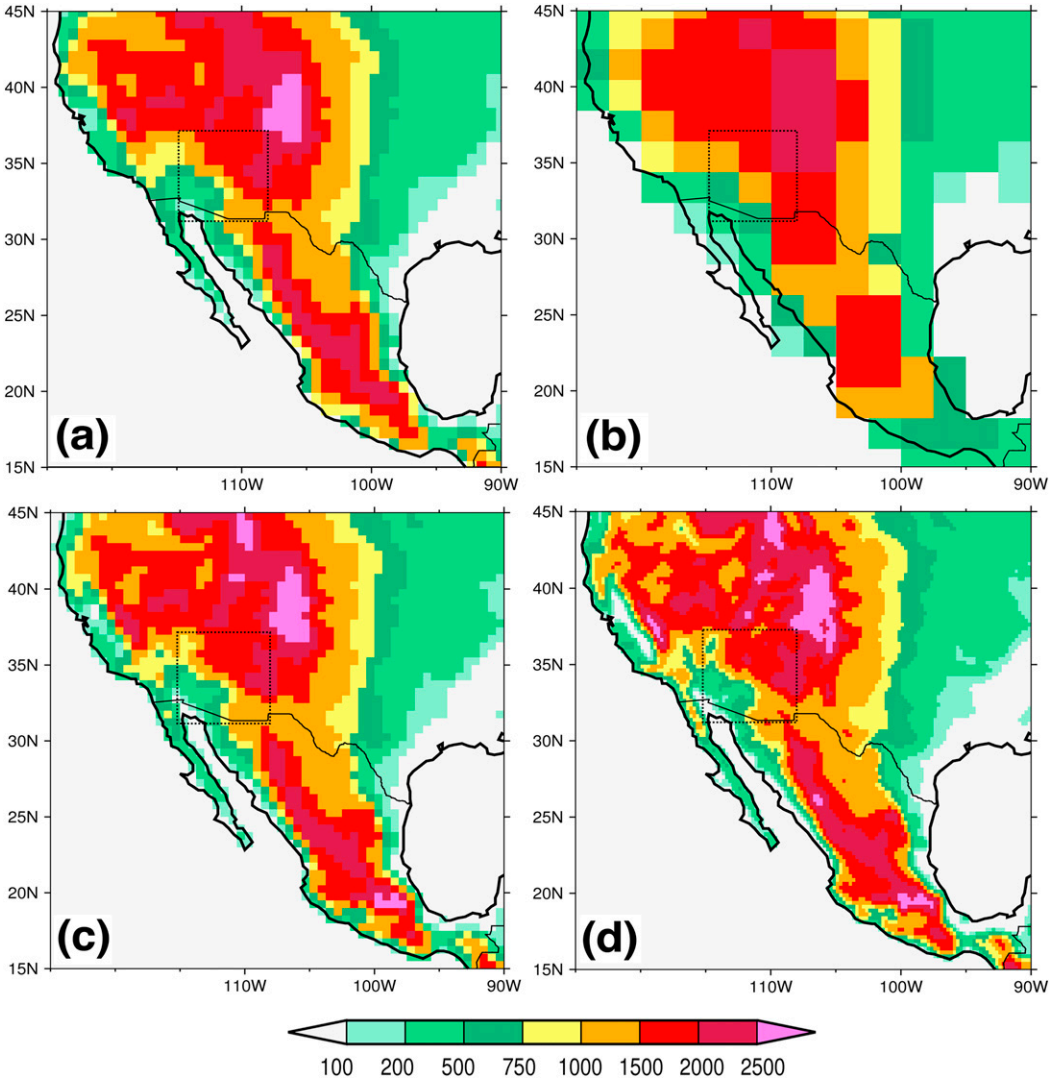

FIG. 1. Surface elevation (m) in (a) ERA-I, (b) CM2.1, (c) FLOR, and (d) HiFLOR. CM2.5 and CM2.6 have the same surface elevation as FLOR. The dashed rectangular box denotes the AZWNM area used for area averaging.

c. *Main NAM climatological features*

Climatologies of mean precipitation, near-surface wind, and 500-hPa geopotential height during the mature monsoon season (July–August) are shown in Fig. 3 for all models. Models that can realistically resolve the GoC also capture the low-level jet, which is, however, absent in CM2.1. On larger scales, most models (FLOR, CM2.5, CM2.6, and HiFLOR) fail to faithfully reproduce the position of the midtropospheric monsoon high, with a common southward bias relative to its observed position over New Mexico. This bias appears to be partly associated with the atmospheric response to SST biases; FLOR-FA, in which flux adjustment greatly reduces errors in SSTs, has a more realistic placement of the monsoon high. Most models overestimate the NAM mean precipitation over northwestern Mexico but do capture the AZWNM precipitation, with the exception of CM2.1.

d. *GoC surge index and regression analysis*

One of the most important and widely used criteria for GoC surge identification is the associated development of low-level northward flow. Therefore, to isolate GoC surge events, we use the index described in Pascale and Bordoni (2016), which is a generalized version of that introduced by Bordoni and Stevens (2006) and is based on the first and second principal components (PC1 and PC2) of an EOF analysis of the temporal covariance matrix (*S* mode) of the summertime "alongshore" GoC near-surface wind. The following algorithm is applied to identify the onset, duration, and end of each individual GoC surge: 1) We determine the days $t = \{t_1, t_2, \ldots, t_n\}$

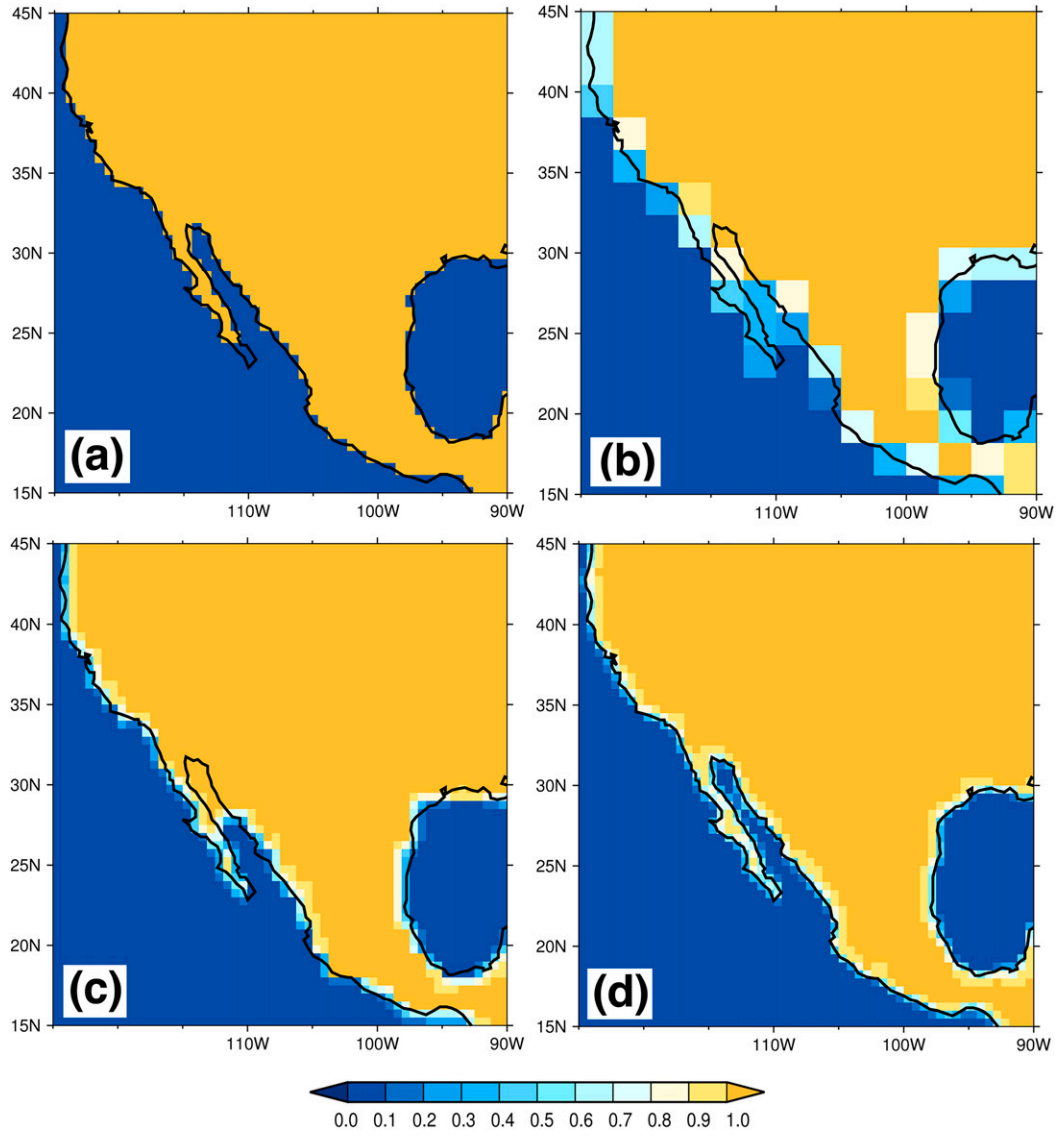

FIG. 2. Land–sea mask field (fraction of land area for each box) in (a) ERA-I, (b) CM2.1, (c) FLOR, and (d) CM2.5. The field for CM2.6 (not shown here) is almost indistinguishable from CM2.5.

for which either PC1 or PC2 is above a given threshold (e.g., 0.75). 2) We then collect all surge days and group them by surge events—that is, $t = \{t_1^{(1)}, t_2^{(1)}, t_3^{(1)}, t_1^{(2)}, t_2^{(2)}, t_3^{(2)}, t_3^{(2)}, \ldots\}$. The last day of a surge event [e.g., $t_3^{(1)}$] and the onset of a successive one [e.g., $t_1^{(2)}$] have to be separated by at least one nonsurge day, for which PC1 and PC2 are both less than 0.75. 3) The onset day of an individual surge event k is therefore $t_1^{(k)}$ and its end $t_m^{(k)}$, where m is the number of days the kth GoC surge lasts. This approach is able to capture both major and minor surge events, which differ in their spatial extent along the GoC.

The alongshore wind is the component of the 10-m wind parallel to the GoC axis, restricted over the GoC (i.e., over an oceanic strip along and slightly south of the GoC from 20° to 32°N). In the case of FLOR, in the definition of GoC grid points we also include those north of 28°N corresponding to low-elevation land surface (rather than ocean). For CM2.1, which does not have a high enough spatial resolution to really resolve the GoC, we incorporate all grid points roughly corresponding to the geographic location of the GoC (31.35°N, 113.75°W; 29.32°N, 113.75°W; 27.3°N, 111.25°W; 25.28°N, 111.25°W; 25.28°N, 108.75°W; 23.26°N, 108.75°W; 23.26°N, 106.25°W; 21.24°N, 108.75°W; and 21.24°N, 106.25°W). The leading PCs of the EOF analysis are robust to slightly different choices of the space domain (Bordoni and Stevens 2006). For all models, PC1 explains

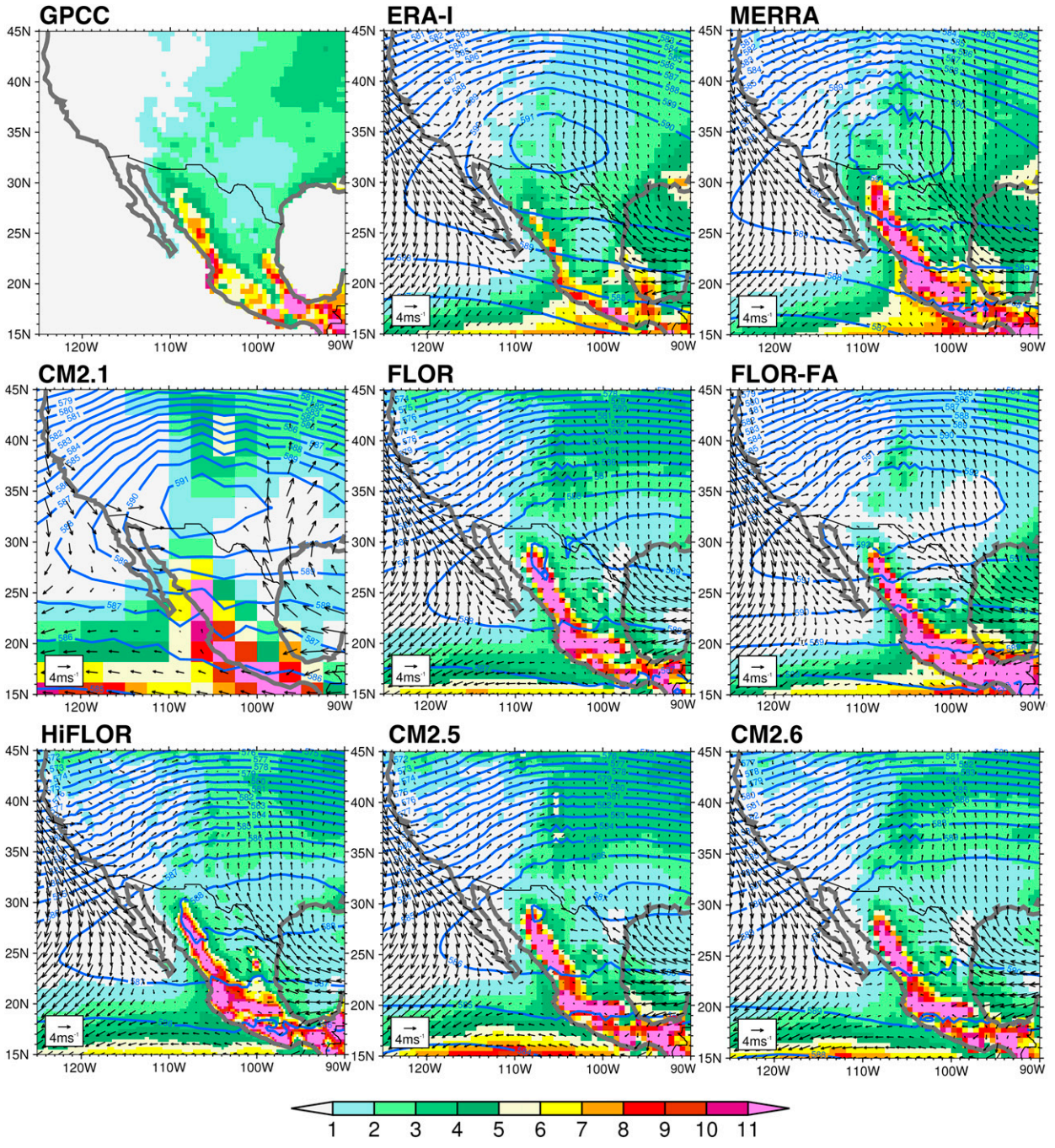

FIG. 3. Climatological July–August (JA) mean precipitation (color shading; mm day^{-1}), 10-m wind (vectors), and 500-hPa geopotential height (blue contours; dam) in observations (1979–2014 in GPCC and ERA-I, 1979–2010 in MERRA) and six GFDL models (100-yr 1990-condition control run). Here we use JA in place of JAS—as done elsewhere throughout this paper—because this period corresponds to the mature monsoon season when the anticyclone is most developed.

around 60% of the variance regardless of resolution (e.g., 66% for CM2.1 and 61% for CM2.5). Therefore, our surge detection method is essentially independent of resolution and able to capture surge events with the same efficiency in all the models considered in this study.

As discussed in Pascale and Bordoni (2016), PC1 is highly correlated (≃0.97) with the domain-averaged alongshore wind anomalies, and thus it provides information on the dominant time variability of GoC summertime wind anomalies as a whole. Figure 4 shows the normalized power spectrum of PC1 from reanalyses

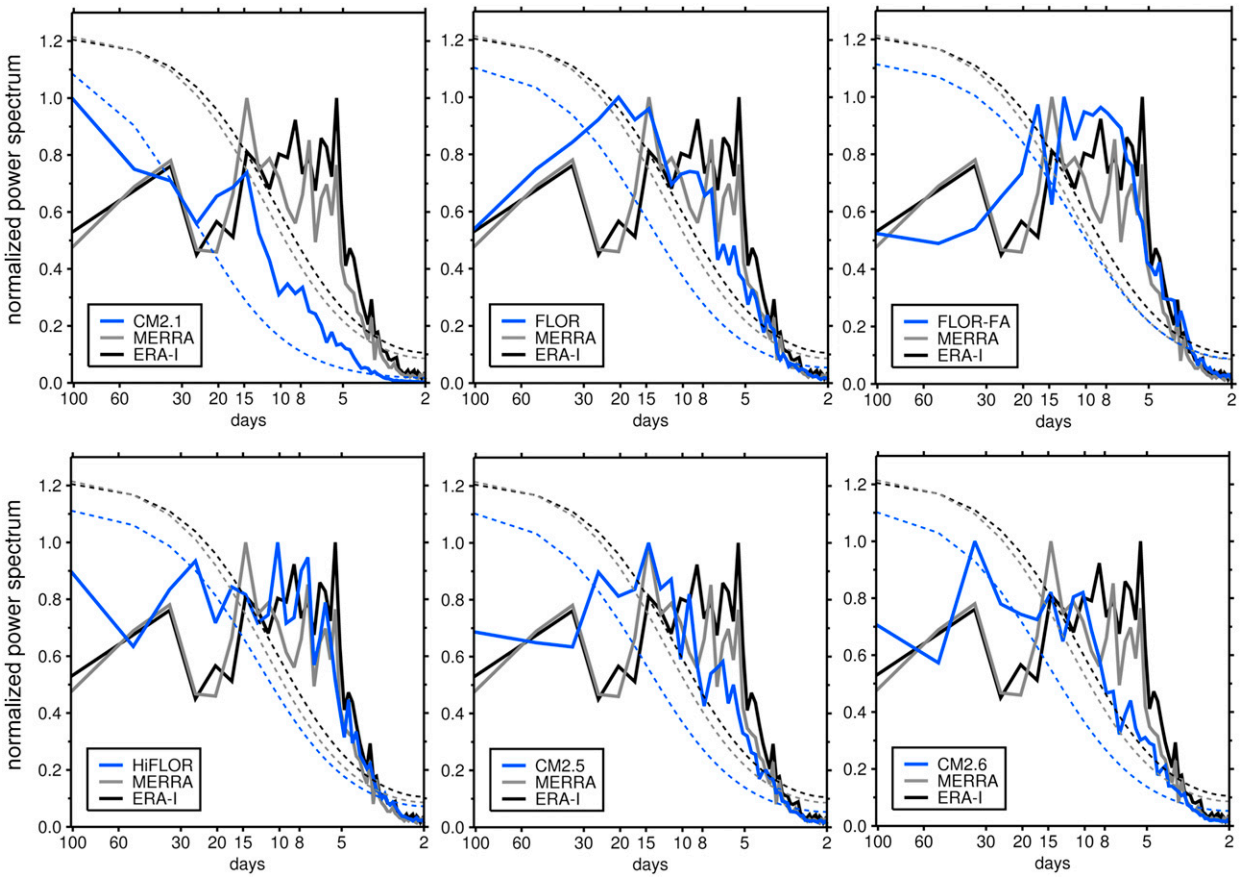

FIG. 4. Normalized power spectrum of PC1 of the summertime alongshore GoC near-surface wind for CM2.1, FLOR, FLOR-FA, HiFLOR, CM2.5, and CM2.6 as compared to reanalyses. The dashed curves denote the 95% a priori confidence limit (Gilman et al. 1963), normalized relatively to the red noise.

and models. It can be seen that increasing model atmospheric spatial resolution (Fig. 4) results in a great improvement in the modeled wind variability in the GoC, particularly at the synoptic time scales (≤10 days). In this time window, the summertime GoC wind variability is mainly associated with the passage of tropical easterly waves (TEWs) or tropical cyclones (TCs)—often triggered by a TEW (e.g., Lorenz and Hartmann 2006)—south of the GoC (Serra et al. 2008, 2010; Corbosiero et al. 2009; Wood and Ritchie 2013). The low energy in the CM2.1 power spectrum at synoptic time scales suggests an overly weak TEW and/or TC variance in CM2.1, consistent with findings in Lin et al. (2008). That the time variability of surges is poorly represented at coarse resolution is not self-evident; while it is reasonable to expect that GoC surge spatial details are not correctly captured in CM2.1 (section 3a), the impact of model resolution on the time variability is less trivial. HiFLOR, which has the highest atmospheric horizontal resolution, successfully captures, at least qualitatively, the structure of peaks between 4 and 8 days seen in the reanalyses (Fig. 4, bottom left). Interestingly, we find that introducing a flux adjustment in FLOR has a similar impact on the simulated variability to that of increasing atmospheric resolution from 50 to 25 km for scales shorter than 7 days (Fig. 4, top center). This may be linked to the southward displacement of the mid-to-upper-level monsoon ridge relative to its observed position (Fig. 3), which in turn might prevent a deeper northward penetration of TEWs over Mexico. Additionally, a southward-displaced monsoon ridge may also prevent upper-level troughs, normally steered along the southern flank of the monsoon high, from reaching northwestern Mexico and the GoC, where they lead to organized convection often associated with minor surges (Adams and Comrie 1997).

To investigate the most common thermodynamical and dynamical patterns associated with GoC surges, we perform lagged regressions of fields of interest on PC1 and PC2 and add them with a −1-day lag [as described more in detail in Pascale and Bordoni (2016)]. Because the standardized PC time series are dimensionless, these regression maps have the same units as the

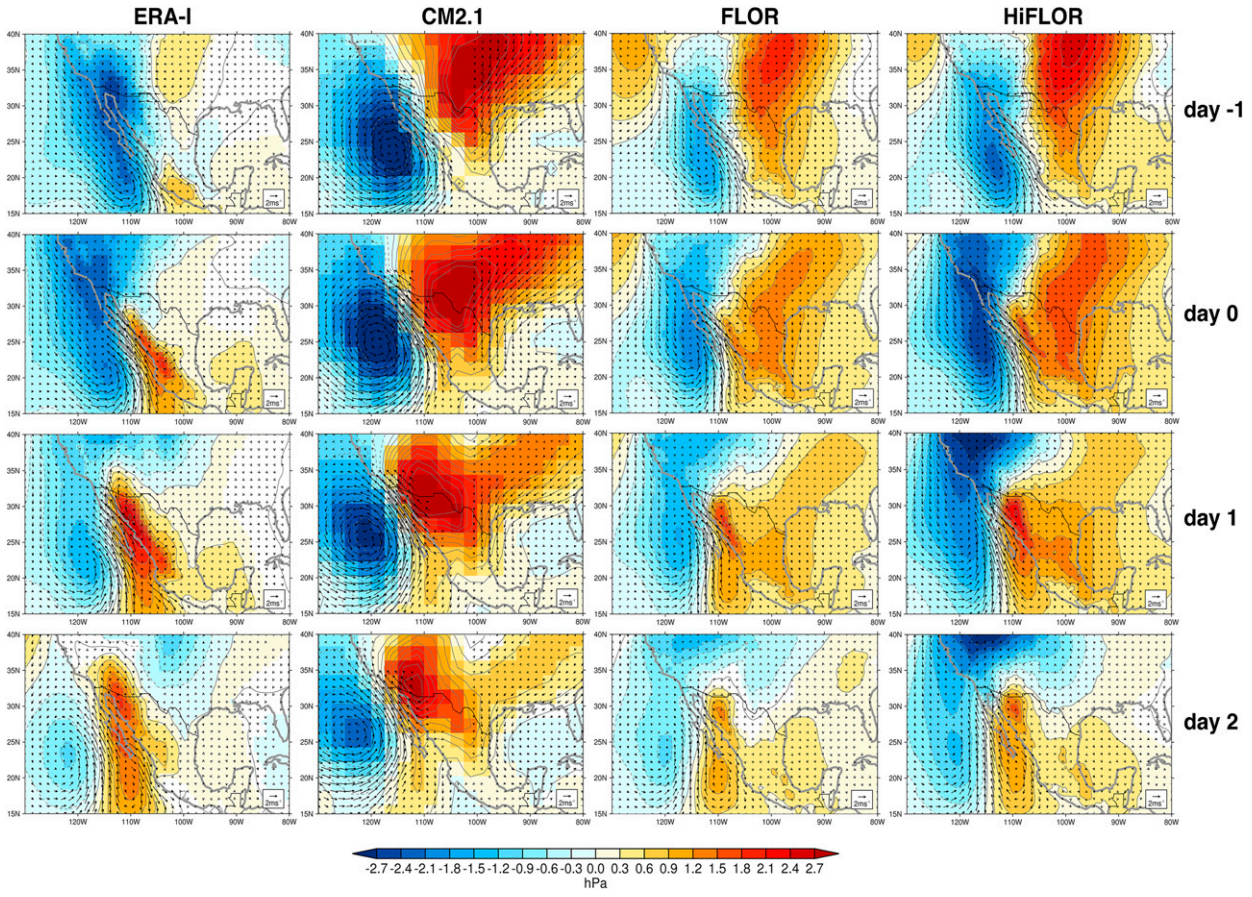

FIG. 5. Lagged regressions of 10-m (925 hPa for CM2.1) wind (vectors; m s^{-1}) and sea level pressure anomalies (color shading and contours; hPa) for ERA-I, CM2.1, FLOR, and HiFLOR. Field values are shown (color shading) only where significant at the 5% level (95%, Student's *t* test).

anomaly field itself, and their amplitudes correspond to anomaly values in that field that occur in association with a one standard deviation anomaly in the independent variable (i.e., the index time series). Specifically, we consider 10-m wind, 10-m specific humidity, total precipitation, and 500-hPa geopotential height and winds. These atmospheric variables are available as daily means for the GFDL models and MERRA. Daily means are obtained for all fields of interest from the 6-h ERA-I data. To isolate synoptic, submonthly, and subseasonal atmospheric variability of the GoC and AZWNM region, the seasonal cycle is removed applying a Lanczos high-pass filter (Duchon 1979) with a cutoff frequency of 100 days (e.g., Kikuchi and Wang 2009). Mean and linear trends are also removed from the time series for the period 21 June–30 September, so all statistics are computed for anomalies relative to the summertime climatology. The choice of this period is justified by the fact that the monsoon onset over AZWNM typically occurs later than 21 June, while the retreat occurs more gradually in late September (Higgins et al. 1997).

Statistics for GoC surges and AZWNM precipitation are presented in terms of the following statistical indicators: minimum, 25th percentile, median, 75th percentile, and maximum. To allow for a more direct comparison between models (100-yr control runs) and reanalyses (36- and 32-yr sequence for ERA-I and MERRA, respectively) we estimate them using bootstrapping with replacement: 30 years are randomly sampled 1000 times and quantiles are computed. Thus, statistical indicators are based on the mean over one thousand estimates.

3. Model intercomparison of GoC surges

In this section we investigate the capability of GFDL models to simulate climatological patterns associated with surge events.

a. Near-surface wind anomalies

We begin with assessing how realistically the different GFDL models capture the near-surface wind anomaly

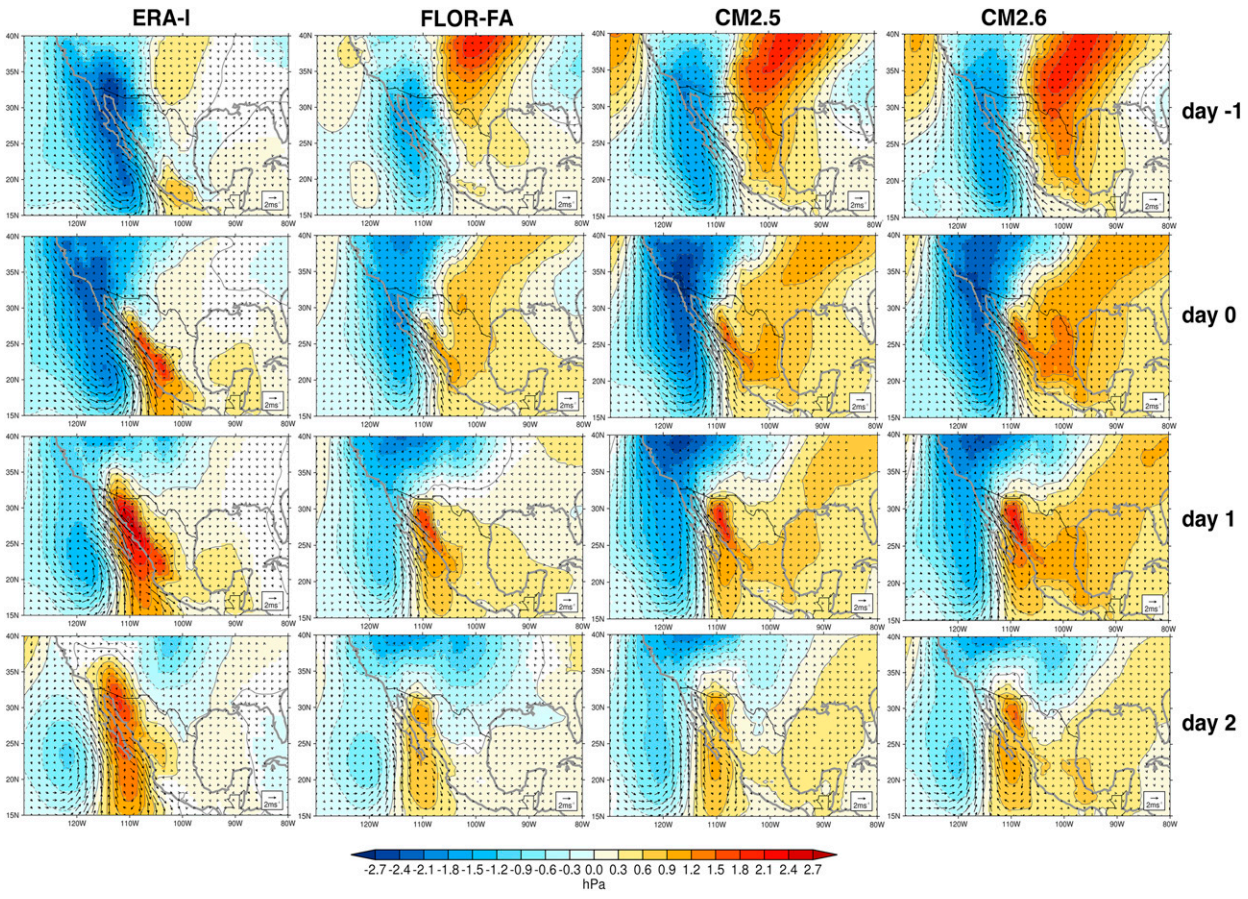

FIG. 5. (*Continued*)

during a surge event. Lagged regressions from day −1 to day +2 of the 10-m wind and sea level pressure anomalies for models and ERA-I are shown in Fig. 5. ERA-I and MERRA feature very similar regression patterns, and hence in the following we will primarily focus on the former.

All models, with the exception of CM2.1, fairly realistically reproduce the strong southeasterly wind anomalies along the GoC seen in ERA-I (Anderson et al. 2000; Berbery and Fox-Rabinovitz 2003; Gochis et al. 2004; Rogers and Johnson 2007; Douglas and Leal 2003). Also evident are a concomitant progression of a TEW, or the passage of a TC (Higgins and Shi 2005; Corbosiero et al. 2009; Wood and Ritchie 2013), to the south of the GoC and a midlatitude westerly disturbance over the central United States (e.g., Pascale and Bordoni 2016). In CM2.1—the model with the lowest resolution—GoC surges do not feature a realistic structure. More specifically, the cyclonic anomaly that supports the development of the strong southeasterly anomalies along the Mexican and GoC coast is too broad, extends too far northward, and tends to last longer than in reanalyses. In this respect, the CM2.1 wind surges more resemble those directly associated with TCs passing close to the southern GoC (Higgins and Shi 2005).

We also note that wind anomalies in FLOR and FLOR-FA are generally weaker over the northernmost part of the GoC. This likely results from the northern GoC being covered by land rather that ocean in these models (Fig. 2), with higher surface drag slowing down the surge as it propagates northward. Interestingly, the increased ocean resolution in CM2.6 (0.1° × 0.1°) relative to CM2.5 (0.25° × 0.25°) does not lead to substantial differences in simulated surge extent and spatial patterns.

We assess GoC surge intensity using the standard deviation of the GoC spatially averaged alongshore wind and 10-m moisture flux anomalies (Figs. 6a,b). Larger values of the standard deviation indicate larger fluctuations—because of wind surges—around the zero mean. The typical observed wind (moisture flux) anomaly for a surge is $\simeq 4\,\mathrm{m\,s^{-1}}$ ($\simeq 8\,\mathrm{g\,kg^{-1}\,m\,s^{-1}}$), as suggested by both ERA-I and MERRA. Box-and-whisker plots of the standard deviation of GoC surge wind anomalies as seen in the different model simulations (Fig. 6a) suggest that simulated surges are generally weaker in terms of near-surface wind

($\simeq 3\,m\,s^{-1}$ in FLOR, CM2.5, CM2.6, and HiFLOR) but have a similar spread around the median. CM2.1 is the only exception, showing both stronger intensity and larger spread. When the surge intensity is instead measured in terms of near-surface moisture flux (Fig. 6b), most models (FLOR, CM2.5, and CM2.6) show a much better agreement with observations. Note that here we use MERRA because the 10-m specific humidity is not available in ERA-I. The compensation in the model near-surface moisture flux is likely due to a warm SST bias ($\simeq 1$ K) during the summer months over the eastern Pacific (see Vecchi et al. 2014). Month-by-month analysis (Figs. 6c,d) reveals that, in reanalyses, the most intense GoC surge-related wind anomalies occur in September ($\simeq 7$ vs $\simeq 4\,m\,s^{-1}$ in July–August). This is most likely due to the passage of TCs south of the Baja California peninsula (Higgins and Shi 2005; Corbosiero et al. 2009; Wood and Ritchie 2013). This seasonal pattern with a maximum in September is also seen in the moisture flux ($\simeq 14$ vs $\simeq 10\,m\,s^{-1}\,g\,kg^{-1}$ in July–August), although less pronounced because of decreasing SSTs and near-surface temperatures in the GoC region at the end of summer (Ripa and Marinone 1989). In general GFDL models—except for CM2.1 and FLOR-FA—capture well the surge-related moisture fluxes with respect to MERRA in July and August but overestimate them in September. HiFLOR features the largest values in September while the most unrealistic behavior is that of CM2.1, which has above-normal moisture fluxes, especially in August. This excess in near-surface surge-related moisture fluxes in the GoC is likely attributable to SST biases in the eastern Pacific (Vecchi et al. 2014), which may compensate for the weaker winds.

While the spatial resolution increase from CM2.1 to FLOR results in a dramatic improvement in the simulation of GoC surges, further resolution increases have a more modest impact. In particular, it is found that increased ocean resolution has very little influence on surge simulations (see CM2.5 and CM2.6 in Fig. 5). It is therefore likely that 50-km resolution in the atmosphere and 0.25° resolution in the ocean is sufficient to represent the main large-scale features of GoC surges. A more noticeable effect is that flux adjustment, which removes SST biases, has a more profound impact on the large-scale atmospheric circulation. While resulting in a weakening of GoC surges, as seen in Fig. 6, the flux adjustment generally improves surge patterns (Fig. 5). We will return to this point in the following sections.

b. *Near-surface moisture anomalies*

A large humidity anomaly, located right over the GoC, typically precedes the arrival of the moisture surge over land (e.g., Rogers and Johnson 2007). Thereafter the anomalous moisture spreads into the southwestern United States. These well-known patterns are well captured by lagged regressions of 10-m specific humidity anomalies from MERRA (Fig. 7). At day −1 (presurge day), a very strong moisture anomaly is visible over the entire GoC and over the surrounding slopes of the Sierra Madre Occidental and Baja California peninsula. As expected, CM2.1, which does not have a resolved GoC, performs the worst, with specific humidity anomalies that are overly broad and displaced westward over the Pacific. The moisture pattern internal to the GoC at day −1 is well reproduced by CM2.5 and CM2.6, which have the highest ocean resolution and the most realistic representation of the GoC. These same models, however, along with FLOR, have overly positive moisture anomalies to the west of the Baja California peninsula, which is likely due to the summertime warm SST bias over the eastern Pacific (Vecchi et al. 2014). FLOR, FLOR-FA, and HiFLOR feature drier conditions in the northern GoC, consistent with their inaccurate representation of the northern GoC as a land surface rather than ocean and associated limitation on surface evaporation (e.g., Mullen et al. 1998; Schmitz and Mullen 1996; Berbery 2001).

At day +1, the moisture anomaly has moved northward into northwestern Mexico (Sonoran Desert) and the southwestern United States (Arizona, western New Mexico, southern Nevada, and southeastern California); these anomalies, however, never extend beyond the mountain ridge dividing the Mojave Desert from the California coastal regions. In all models, the positive anomaly over the southwestern United States is displaced eastward and is excessively elongated northeastward as compared to reanalyses. The northeastward elongation of the moisture anomaly appears to be linked to an overly strong midlatitude westerly disturbance phasing with the GoC surge, which allows for a farther northeastward spreading of the southerly moisture anomaly. This moisture bias could also be related to the poorly resolved Rocky Mountains (even in HiFLOR), which allows excessive moisture originating from the eastern Pacific to penetrate over the southern Great Plains. In spite of their lack of the northern GoC moisture source, FLOR and HiFLOR still have GoC surge-related specific humidity anomalies similar to those seen in CM2.5 and CM2.6. We speculate that this is due to the above-discussed warm SST bias in the eastern Pacific Ocean, which leads to a surplus of moisture available for northward transport and counteracts the drying effect owing to missing ocean conditions in the northern GoC. Otherwise, this could suggest that moisture is primarily advected from farther south rather than locally reinforced by evaporation. As seen in the low-level flow (section 3a), and in spite of the obvious limitations due to an incomplete

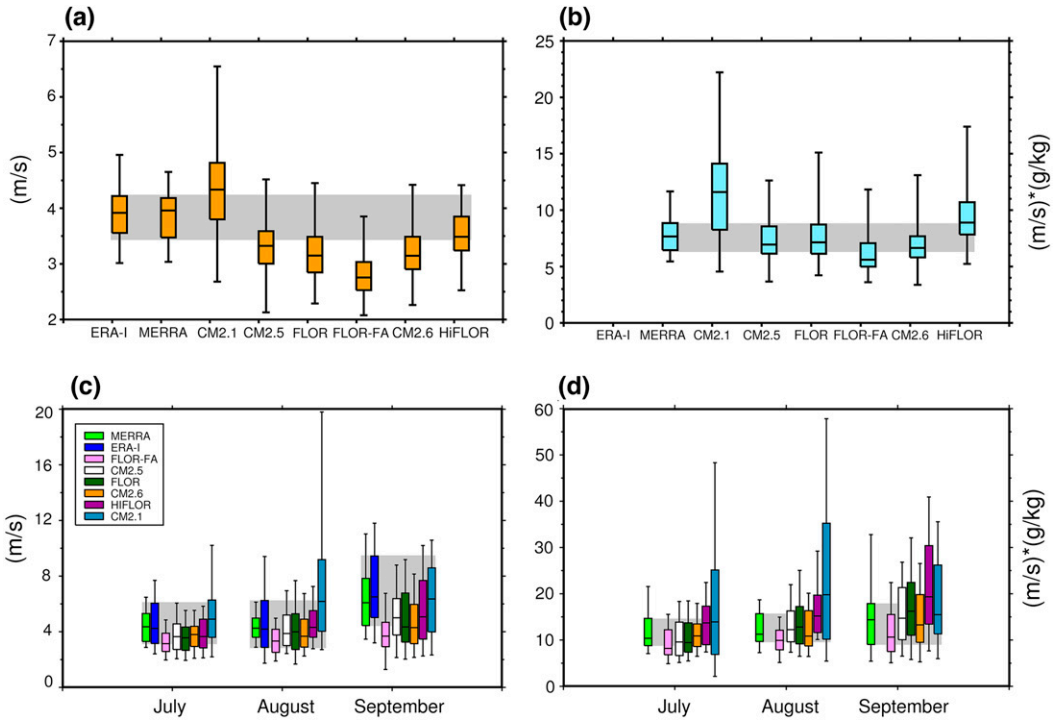

FIG. 6. Box-and-whisker diagrams (minimum; 25th, 50th, and 75th percentiles; and maximum) summarizing the interannual variability of (a) JAS standard deviation of area-averaged GoC alongshore wind anomalies. The time series is built by taking daily alongshore wind anomalies from June to September and spatially averaging them over the GoC. For each year, the standard deviation of this time series is a measure of the amplitude of the southward–northward upturning associated with surges; (b) as in (a), but for 10-m moisture flux anomalies. (c) Mean peak wind reached during wet surge days (see definition in section 2d). The mean peak wind is estimated, for each month and for each year, as the mean (among all wet surge events occurring in that month) of the largest spatially averaged alongshore wind anomaly during a wet surge event; (d) as in (c), but for 10-m moisture flux. The gray shading denotes the maximum (minimum) 75th (25th) percentile between the two reanalyses, and it is shown to help compare the different boxes.

representation of the GoC, FLOR-FA appears to be the best-performing model, as compared to reanalyses.

c. *Precipitation anomalies*

Lagged regression maps of precipitation anomalies (mm day^{-1}) at day −2 and day +1 are shown in Fig. 8. At day −2, ERA-I shows a dry anomaly over the NAM region and the western United States, while the well-documented (e.g., Bordoni and Stevens 2006; Seastrand et al. 2015) positive precipitation anomaly associated with the passage of a TEW or a TC to the south of Mexico is evident south of the GoC. On the larger scale, the typical negative correlation pattern between the southwestern and central-eastern United States is observed (e.g., Mullen et al. 1998; Mo 2000). Lagged regressions based on MERRA show very similar results (not shown). These patterns are overall captured well by the high-resolution models (FLOR, HiFLOR, CM2.5, and CM2.6). Not surprisingly, CM2.1 is again the poorest-performing model, in that it only captures the broad large-scale precipitation anomalies at low latitudes (associated with the TEW) and at higher latitudes (associated with midlatitude disturbances) but performs very poorly over the GoC region, with broad and westward-extending precipitation anomalies.

At day +1, ERA-I and the models feature above-average anomalous precipitation (≥1 mm day^{-1}) over northwestern Mexico and the southwestern United States, attributable to the low-level moisture inflow associated with GoC surges. The anomaly extends up to 40°N, which is traditionally considered as the northernmost climatological limit of the NAM rainfall (Adams and Comrie 1997). Although this signal is captured in CM2.1, its extent is not realistic, with too much rainfall over California. This bias may be attributable to the lack of the channeling effect of the GoC and the Gila–Colorado basin in southwestern Arizona, which allows surges to propagate northwestward. Interestingly, ocean resolution does not have a large impact on the surge-related precipitation; FLOR and CM2.5, for example, have very similar anomalous rainfall patterns over the

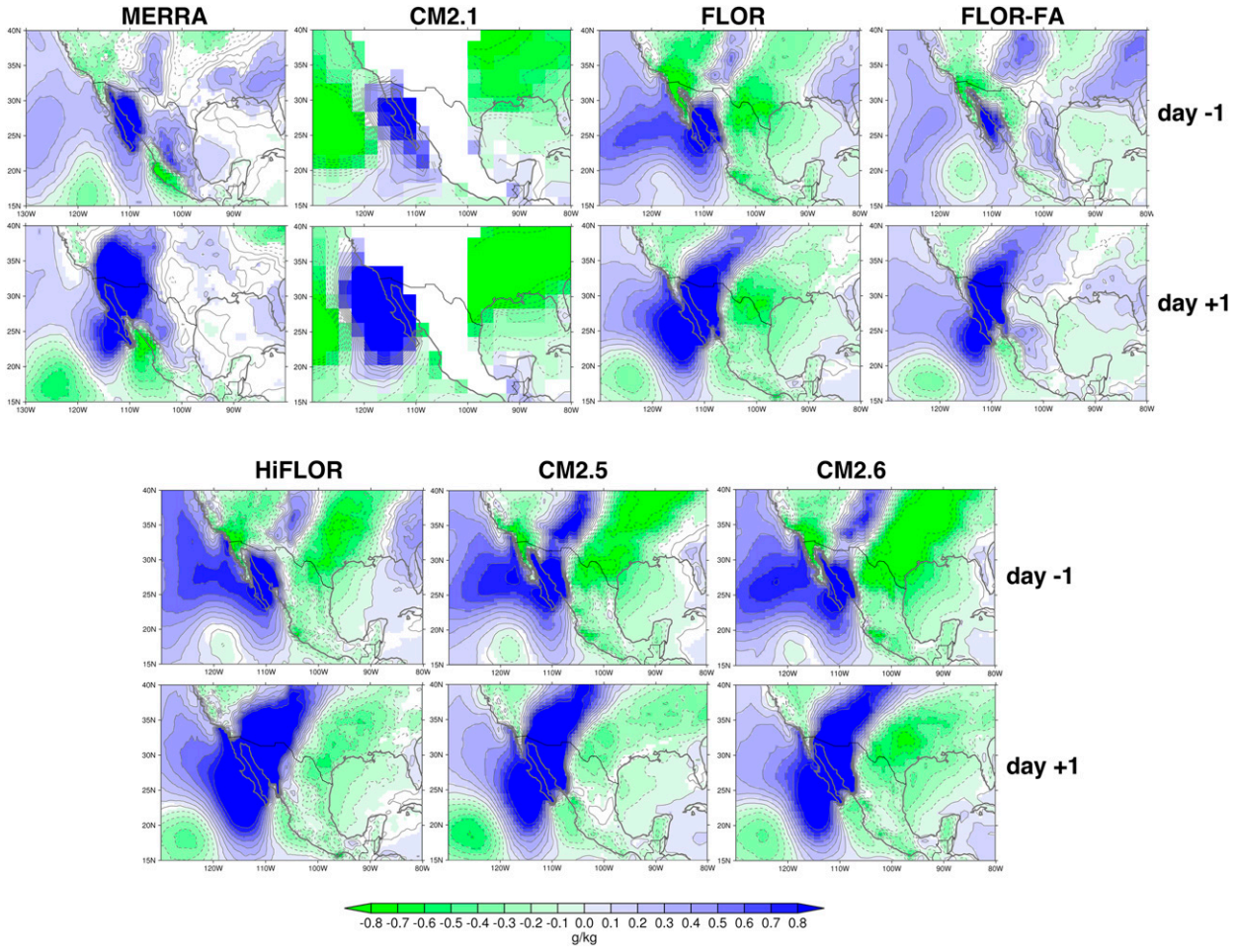

FIG. 7. Lagged regressions of 10-m (925 hPa for CM2.1) specific humidity anomalies (g kg^{-1}) for MERRA and the six GFDL models. Field values are shown (color shading) only where significant at the 5% level (95%, Student's *t* test).

southwestern United States in spite of their different ocean resolutions. This suggests that a correct and realistic representation of the topography of the monsoon region is more important than a realistic representation of the land–sea fraction and ocean dynamics. Future targeted simulations with idealized boundary conditions will further clarify the role that boundary conditions play in shaping the NAM and its synoptic-scale variability.

FLOR-FA has drier surges over AZWNM. This is likely due to the reduction of moisture anomalies over the tropical eastern Pacific Ocean (Fig. 7), which is in turn due to the strong reduction of the warm SST bias. Furthermore, the inaccurate representation of the northern GoC (with land surface rather than ocean) may also contribute to decreased precipitation in this region since the northern GoC is an important moisture source for Arizona's summertime rainfall (Mullen et al. 1998; Schmitz and Mullen 1996; Berbery 2001; Erfani and Mitchell 2014). We also note that models miss the southward extent of the rainfall anomaly over Mexico seen in ERA-I at day +1. This may be related to the southward displacement of the monsoon ridge (Fig. 3), which might prevent upper-level troughs to pass over this region (e.g., Bieda et al. 2009; Finch and Johnson 2010). In FLOR-FA, which better reproduces the climatological position of the monsoon high, this bias is less severe. Future research will be aimed at more systematically assessing the climatology of upper-level inverted troughs in these models.

d. Surge statistics and AZWNM precipitation

Following Higgins et al. (2004), we further characterize the statistical relationship between surges and precipitation over AZWNM. Here we use the definition of wet and dry surges as in Pascale and Bordoni (2016): if the spatially averaged mean precipitation over AZWNM associated with a surge event is greater than the mean July–September (JAS) AZWNM precipitation, we

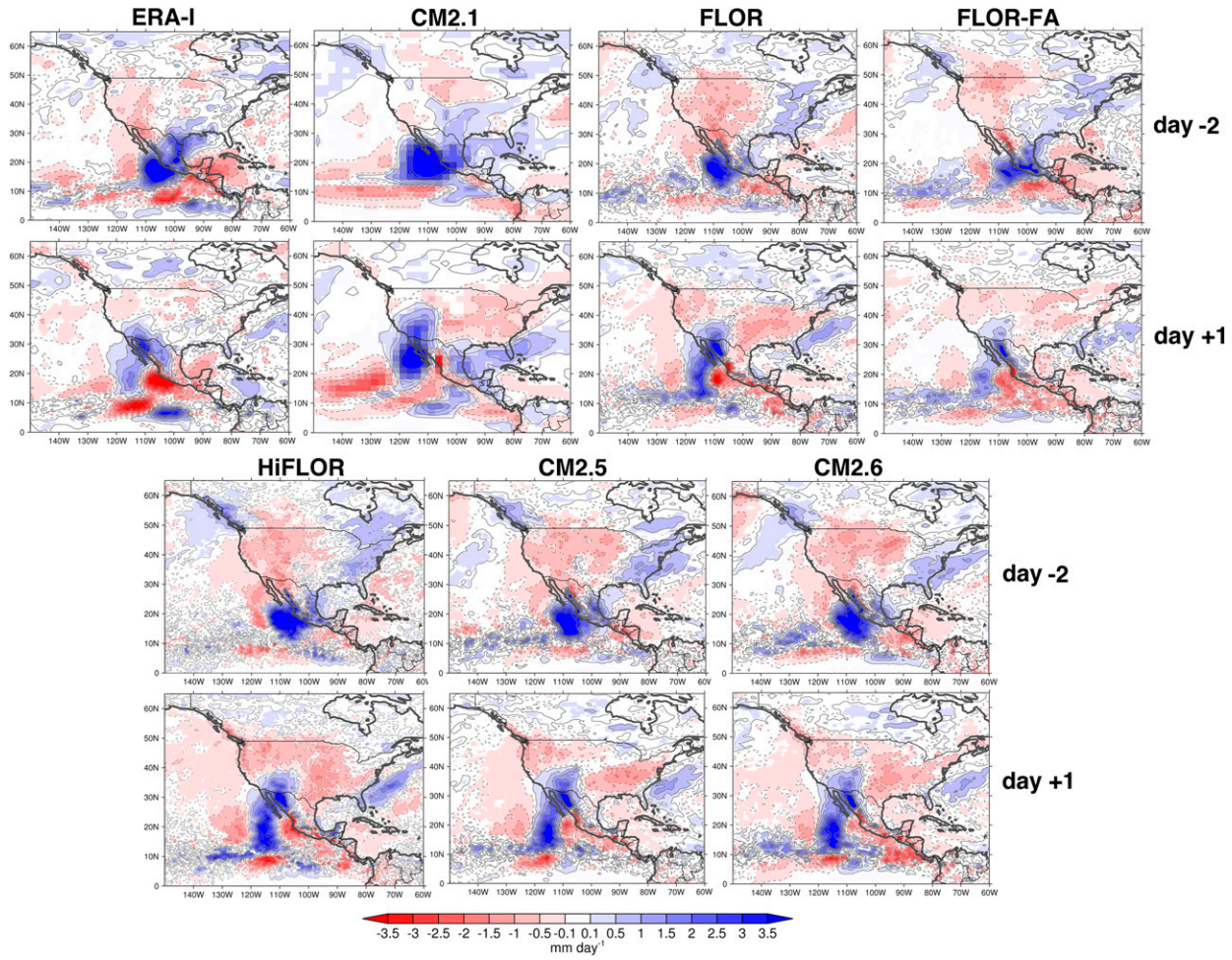

FIG. 8. Lagged regressions of total precipitation anomalies (mm day^{-1}) for ERA-I and the six GFDL models. Field values are shown (color shading) only where significant at the 5% level (95%, Student's *t* test).

define the surge as wet; otherwise we define it as dry. Results are robust to changes in chosen threshold (e.g., 1.5 or twice the JAS AZWNM mean). In Fig. 9a we show the spatially averaged JAS precipitation over AZWNM and the contribution by wet surges for the two reanalyses (ERA-I and MERRA) and six GFDL models. We also include (when possible) values from the gauge-based GPCC gridded dataset. All models are broadly drier than GPCC. Between the two reanalyses, MERRA is closer to GPCC values, whereas ERA-I does not perform better than most GFDL models. However, models generally feature a larger interannual spread, with CM2.1 being the most extreme case with some almost completely dry years (close to the minimum in the box-and-whisker diagram) and some unrealistically wet years ($\simeq$3 mm day^{-1}). In spite of the intermodel differences in the JAS AZWNM rainfall, the contribution by wet surges in all models has median values close to reanalyses.

Another aspect to assess is the extent to which models reproduce mean AZWNM monthly rainfall (precipitation peak in August; Fig. 9c). A drier July and August and an overly wet September is a common bias in all models investigated in this paper. The only exception is FLOR-FA, which is drier throughout the summer. CM2.1 has a delayed seasonal cycle, with a precipitation peak in September (Liang et al. 2008; Lin et al. 2008). This raises the question: Are these biases due to surge-related or surge-unrelated precipitation? If the former, does this result from too many simulated surges? Or rather from excessively wet simulated surges? To answer these questions, we estimate the surge-related precipitation—that is, the precipitation accumulated during surge days (Fig. 9d). In CM2.1, precipitation biases are clearly related to surges, which are too dry during July and too wet during September. In the case of FLOR, HiFLOR, CM2.5, and CM2.6, July surge-related precipitation is generally biased low, and

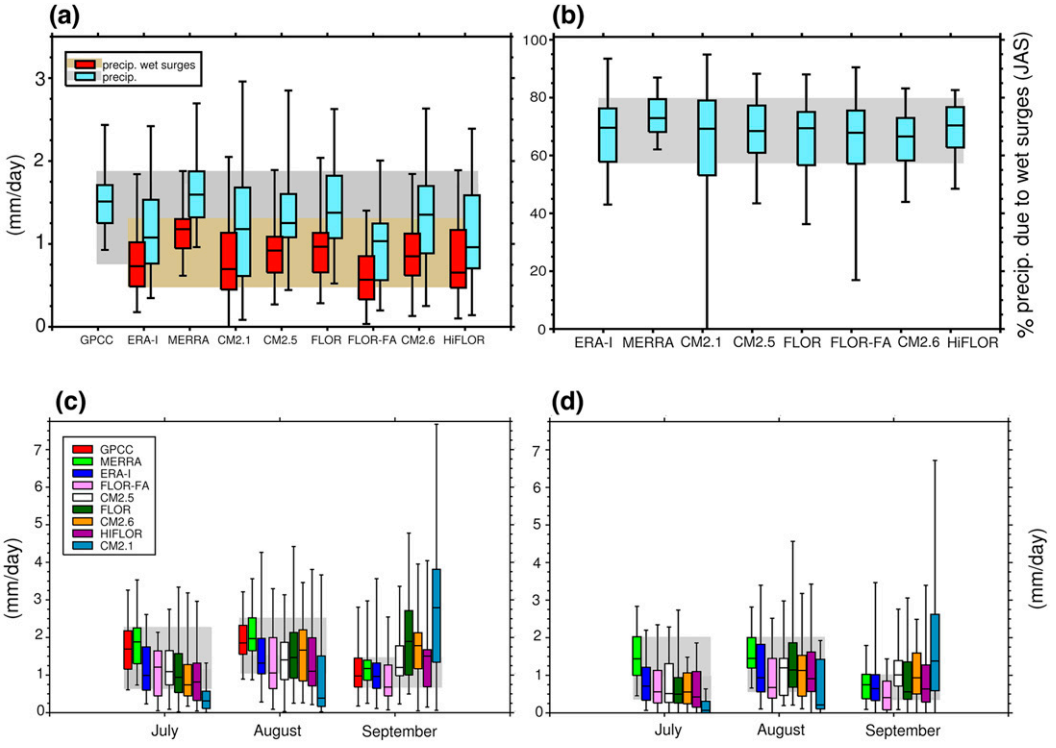

FIG. 9. Box-and-whisker diagrams (minimum; 25th, 50th, and 75th percentiles; and maximum) of (a) mean JAS precipitation and surge-related JAS precipitation over AZWNM; (b) percentage of JAS AZWNM precipitation due to wet surges; (c) seasonal summertime distribution of AZWNM precipitation; and (d) seasonal summertime distribution of AZWNM surge-related precipitation for reanalysis and six GFDL models (Table 1). The gray and gold shading denotes the maximum (minimum) 75th (25th) percentile between the two reanalyses, and it is shown to help compare the different boxes.

September surge-related precipitation remains too large and comparable to that in August.

To better elucidate the reason for these seasonal precipitation biases, in Fig. 10 we show the (climatological) mean distribution (minimum; 25th, 50th, and 75th percentiles; and maximum) of number of surges. When considering the climatological mean over the whole summer (Fig. 10a), the models agree well with observations on the number of total (wet and dry) surges, only slightly underestimating it in the month of July (Fig. 10c). The only exception is CM2.1, which substantially underestimates the annual number of surges (11 vs 15), consistent with the insufficient synoptic-scale variability of PC1 (see Fig. 4). Models tend to slightly underestimate the percentage of wet surges (~55%), especially if compared to MERRA (75%; Fig. 10b). ERA-I and MERRA generally show a good level of agreement. One interesting exception is the number of wet surges in July, which is higher in MERRA than in ERA-I. This is consistent with a drier bias in July in the latter product. FLOR-FA well reproduces the seasonal cycle of number of total and wet surges. All models underestimate the number of wet surges in July (≃2 vs ≃3–4) and August (≃3 vs ≃4). This therefore appears to be related to the model dry bias during these months. However, FLOR, HiFLOR, CM2.5, and CM2.6 have a number of wet surges in September similar to what seen in reanalyses (≃2). This suggests that the wet bias in September seen in these models cannot be attributed to an excess in number of surges, as it is the case for CM2.1, for which wet surges are almost absent in July (≃0–1) and reach a maximum in September (≃2). Therefore, the positive precipitation bias arises primarily from an overly large simulated moisture flux, as evident in Fig. 6d, rather than an overly large number of wet surges. Underestimation of July rainfall and overestimation of September rainfall seen across most of the analyzed models (except for FLOR-FA) are also common features in CMIP3 and CMIP5 models. This is due to a North Atlantic subtropical high that is overly extended toward Central America in July–August, resulting in an overly strong low-level zonal jet to the north of the ITCZ. This diverts tropical moisture away from the monsoon region. During the late monsoon season, the northeastward retreat of the North Atlantic subtropical high steers the anomalously strong

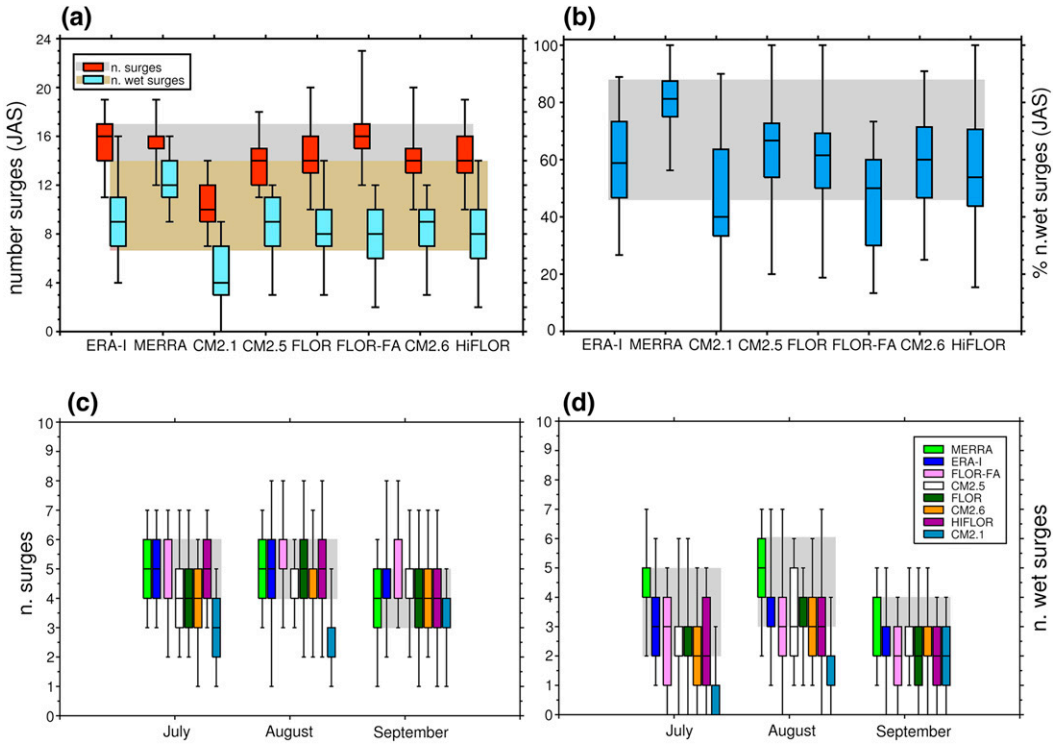

FIG. 10. Box-and-whisker diagrams (minimum; 25th, 50th, and 75th percentiles; and maximum) of (a) mean number of total and wet surges; (b) percentage of wet surges; (c) JAS number of surges; and (d) JAS number of wet surges for reanalysis and six GFDL models (Table 1). The gray and gold shading denotes the maximum (minimum) 75th (25th) percentile between the two reanalyses, and it is shown to help compare the different boxes.

easterly low-level jet along the Mexican coast, thus creating an unrealistic northward tropical moisture transport that makes it difficult for models to realistically capture the timing of the monsoon retreat (Geil et al. 2013).

4. Large-scale tropical and extratropical controls

In this section, we explore the modeled relationship between GoC surges and their large-scale environment. Large-scale tropical and extratropical disturbances are known to affect GoC surges and moisture along the GoC (Lorenz and Hartmann 2006; Kikuchi and Wang 2009; Wu et al. 2009; Pascale and Bordoni 2016). In particular, the initiation of a GoC surge is linked to the passage of a TEW trough across southwestern Mexico at around 15°–20°N (Stensrud et al. 1997; Anderson et al. 2000; Higgins et al. 2004; Schiffer and Nesbitt 2012; Seastrand et al. 2015). In the northernmost, marginal NAM regions, such as the southwestern United States, trans-Pacific midlatitude Rossby wave trains (RWTs) determine the extent to which a surge is followed by positive (wet surge) or negative (dry surge) precipitation anomalies. In fact, Rossby wave energy reshapes the NAM mid-to-upper-level anticyclone, shifting its maximum to the northeast and eroding the anticyclonic ridge over the U.S. West Coast; this pattern favors the intrusion of moist unstable midlevel air from the Gulf of Mexico into the southwestern United States (e.g., Kiladis and Hall-McKim 2004; Higgins et al. 2004; Jiang and Lau 2008; Ciancarelli et al. 2013; Pascale and Bordoni 2016). Furthermore, upper-level inverted troughs of midlatitude origin propagating westward along the southern flank of the upper-level NAM ridge also play a role in organizing NAM convection (e.g., Bieda et al. 2009; Finch and Johnson 2010).

The time evolution from day −2 to day +2 of the 500-hPa lagged regressed wind anomalies and geopotential height for ERA-I (Fig. 11) shows the westward progression of a cyclonic anomaly, elongated from the eastern Pacific to the Caribbean Sea, into the GoC. This anomaly is associated either with a convectively coupled TEW intensifying over the equatorial North Pacific Ocean and then moving on a southeasterly trajectory along the coast of Mexico (Serra et al. 2010) or directly with a TC triggered by a TEW. Given its extension into the Gulf of Mexico, northeast Mexico, and Texas, which

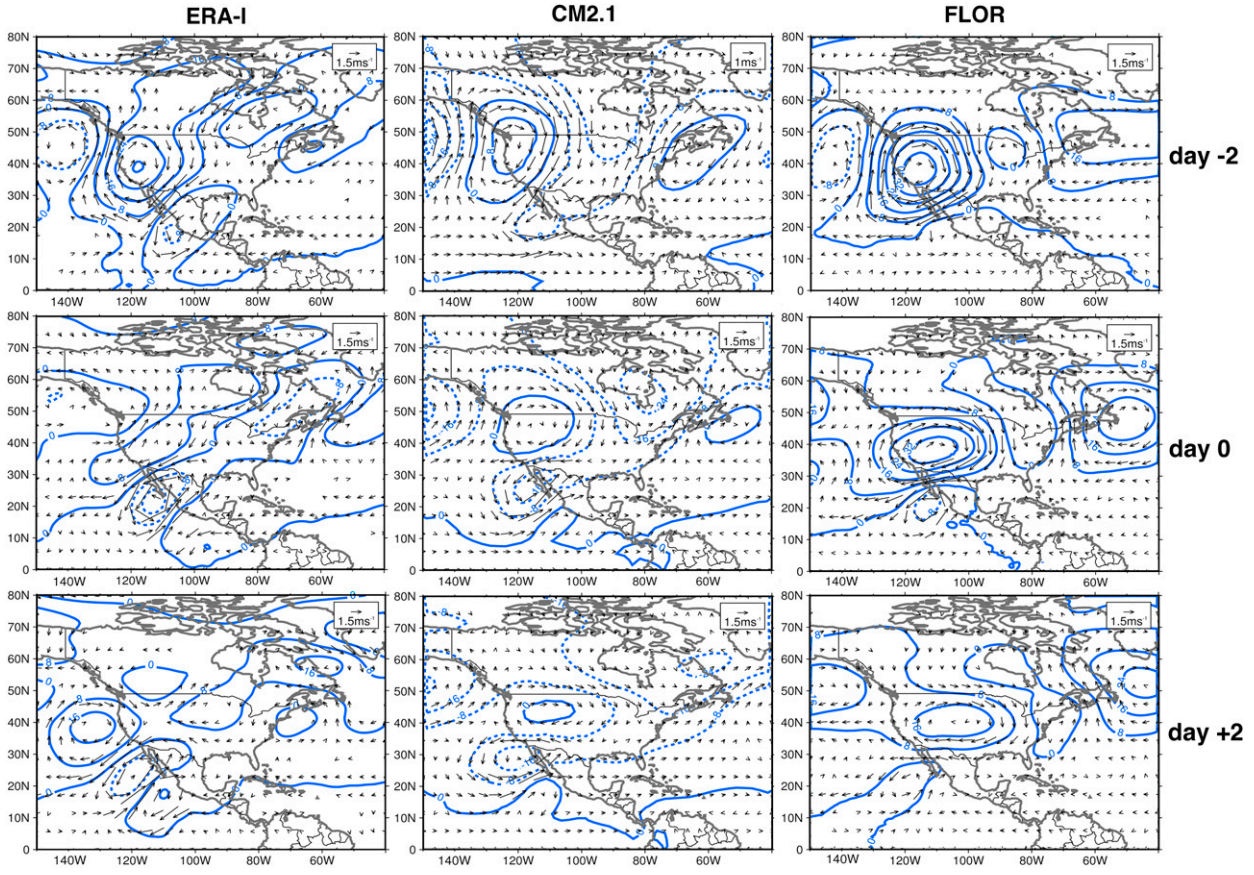

FIG. 11. Lagged regressions of 500-hPa wind (vectors) and geopotential height (blue contours; m) anomalies for ERA-I and the GFDL models CM2.1, FLOR, FLOR-FA, HiFLOR, and CM2.5. Vector fields are shown only where significant at the 5% level (95%, Student's *t* test).

are regions generally not affected by eastern Pacific TCs (e.g., Corbosiero et al. 2009), the 500-hPa anomaly likely indicates the concomitant passage of an upper-level inverted trough (Bieda et al. 2009; Finch and Johnson 2010; Pytlak et al. 2005; Newman and Johnson 2012a). In midlatitudes (around 40°–50°N), the anomalous high over the western United States is strengthened by the arrival of a trans-Pacific RWT prior to the surge event (day −2). As this RWT interacts with the tropical trough and propagates farther eastward, the anomalous high gets elongated along a southwest–northeast axis (day 0) and then splits in two lobes (day +2), one over the eastern Pacific and one over the central United States. A detailed frequency analysis of this evolution can be found in Pascale and Bordoni (2016). This RWT-driven rearrangement of the midlatitude geopotential height anomalies, in synergy with the westward propagation of the upper-level trough, leads to a mid-to-upper-level southeasterly anomalous flow into the southwestern United States in the days following the surge onset (e.g., day +2 in Fig. 11), which further destabilizes the atmosphere resulting in widespread convective activity over the region (Fig. 8).

The large-scale structure of the propagating RWT and TEW or TC revealed by reanalyses is broadly captured by all models. As for previous fields, FLOR, CM2.5, HiFLOR, and CM2.6 show similar patterns; more significant differences exist in CM2.1 and FLOR-FA. While the midlatitude RWT is fairly well represented in its main features (position of the ridges and troughs, propagation, etc.), CM2.1 appears more deficient in reproducing the westward-propagating TEW-related cyclonic anomaly as it transits over northern Mexico and the GoC, both in its shape and position, being overly displaced to the northwest of the GoC during the surge event (day 0 and day +2). In all other high-resolution GFDL models (FLOR, HiFLOR, CM2.5, and CM2.6), GoC surge-related TEWs and TCs are generally too weak, or too infrequent, relative to the RWT, as can be noted by comparing the respective magnitude of the pressure and wind anomalies at lower and middle levels. TEWs in this region result from

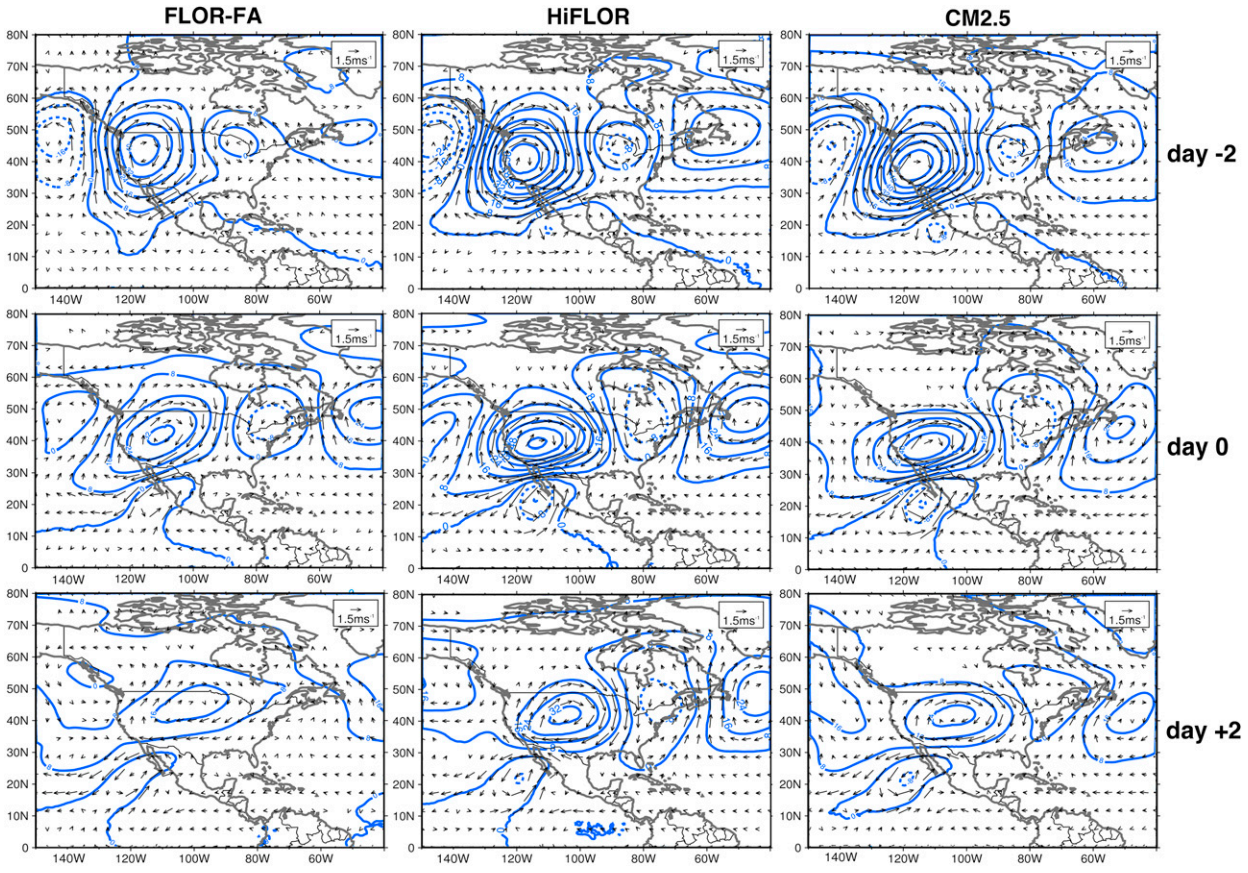

FIG. 11. (*Continued*)

interactions between convective diabatic heating, the Caribbean low-level jet, and the Central American topography (Molinari et al. 1997; Serra et al. 2008; Kiladis et al. 2009; Serra et al. 2010). Thus, the model bias might result from a combination of all of these factors. Inspection of the Caribbean low-level jet reveals that this tends to be more intense (i.e., more easterly) in all models except FLOR-FA over both the Caribbean Sea and the eastern Pacific (not shown), consistent with mechanisms that make it difficult for the models to correctly capture the timing of the monsoon retreat (Geil et al. 2013). Thus, as in the case of the easterly MJO phase, which inhibits cyclogenesis over the eastern Pacific (Maloney and Hartmann 2001; Aiyyer and Molinari 2008), we speculate that a too-strong Caribbean low-level jet also inhibits TEW activity over the eastern Pacific.

Another bias common to all models is a southward displacement of both the cyclonic anomaly over northern Mexico and the anticyclonic anomaly over the western United States. This systematic southward displacement is less severe in FLOR-FA and CM2.1, which have a more realistic placement of the upper-level monsoon high around 30°–35°N in midsummer. Again, this may be related to the southward-displaced monsoon ridge, which in turn may inhibit the penetration of upper-level inverted troughs into northern Mexico.

Hovmöller diagrams of the lagged regressed meridional wind, shown in Fig. 12, allow us to compare the mean features of the tropical and extratropical wave packets over the entire Pacific domain in relation to surge events. Two reference latitudes of 40° and 15°N have been chosen in order to capture midlatitude and tropical waves, respectively. The onset of the surge event (marked with a black dot in Fig. 12) follows the passage of the RWT over North America and coincides with the arrival of the TEW cyclonic center to the south of the Baja California peninsula tip at 100°W, which then leads to positive meridional wind anomalies over the GoC region. Overall, the models reproduce fairly well the timing and the phasing of these two large-scale waves, precursors of GoC surges. CM2.1 again appears as the most deficient model, in that it displaces the RWT westward relative to observations. We also note that TEWs are weaker, compared to the RWT, than those in

reanalyses, not only over the eastern Pacific but over the entire longitudinal domain (100°E–40°W). This seems to be consistent with the global spectral analyses of tropical waves by Murakami et al. (2015).

Compared to reanalyses, over the Pacific (west of 120°W) the midlatitude RWT preceding the GoC surge tends to be dominated by standing waves rather than traveling waves (e.g., Watt-Meyer and Kushner 2015) in most models (CM2.1, FLOR, CM2.5, CM2.6, and HiFLOR). We also note that the second RWT (from day +4 to day +6) reaching western North America and responsible for the northwestward rearrangement of the anomalous high from the western United States to the south of Alaska is much weaker in all models. Overall, FLOR-FA has the most realistic tropical and extratropical wave patterns. Further research is needed to elucidate the impact of SST biases on the extratropical RWTs and associated teleconnections.

5. Discussion

In this section we provide some discussion on the most important implications of horizontal resolution and SST biases for the simulation of GoC surges as they emerge from this study.

a. Horizontal resolution

Simulations of near-surface fields (wind, specific humidity, and precipitation) associated with GoC surges are drastically improved when atmospheric horizontal resolution is increased from 200 (CM2.1) to 50 km (FLOR) while keeping the ocean resolution unchanged. This is consistent with previous work on the summertime mean GoC low-level jet (Mo et al. 2005). Relatively smaller changes are seen when the atmospheric resolution is further increased to 25 km (HiFLOR), although the improved representation of the NAM topographical features generally leads to better accounting of TEWs and precipitation patterns. Higher ocean resolution (FLOR, CM2.5, and CM2.6) allows for a more realistic representation of the GoC, resulting in a deeper northward penetration of GoC surges—otherwise slowed down by land conditions (e.g., FLOR)—and a better representation of moisture originating from the northern GoC (Schmitz and Mullen 1996; Berbery 2001). Therefore, atmospheric resolution impacts GoC surge simulations by 1) allowing the GoC topographical features to be resolved and therefore allowing for moisture of tropical origin to be channeled northward into the northern monsoon region and 2) resulting in more accurate representation of how TEWs and TCs affect the variability of the near-surface flow over the GoC. In other words, the Baja California peninsula and the GoC allow for an extension of the atmospheric variability of the tropical Pacific and the warm tropical SSTs into extratropical latitudes, shielding the influence of near-surface flow and SSTs of the outer midlatitude Pacific Ocean. Concerning the extratropical teleconnections, the surge-related RWT is instead less sensitive to horizontal resolution, being a large-scale and even circumglobal pattern (Kiladis and Hall-McKim 2004; Ding and Wang 2005; Jiang and Lau 2008; Ciancarelli et al. 2013; Pascale and Bordoni 2016).

Finally, a higher horizontal resolution also results in a more realistic representation of topography over AZWNM, where summer convective activity develops over high-elevation terrains (Balling 1987; King and Balling 1994). Therefore, we speculate that part of the negative CM2.1 precipitation bias may be due to the more smoothed terrain in CM2.1, in addition to the lack of a GoC, that in turn disfavors convection. While the high terrain over Arizona provides a strong forcing to thunderstorm formation, and hence needs to be realistically represented, we would also argue for a dominant role of the GoC, which acts as a channel for moisture advection into the region. Future work, involving idealized simulations, is therefore needed to assess and isolate the contribution of resolution and topography versus proper GoC representation.

Near-surface GoC surge features and their large-scale forcings (TEWs, TCs, and RWTs) do not appear to be significantly affected by increased ocean resolution and, with it, by a finer representation of the GoC, as similar patterns are observed in CM2.5 and CM2.6. This allows us to conclude that from an oceanic perspective the GoC impacts the NAM primarily by acting as a low-level moisture source, owing to its very warm SSTs ($\gtrsim$28°C; e.g., Erfani and Mitchell 2014). A more realistic representation of the GoC oceanic circulation, through improved resolution of mesoscale eddies, does not seem to be playing any significant role in NAM simulations.

b. SST biases

Comparison of FLOR and FLOR-FA highlights the role of SST biases (Vecchi et al. 2014) on NAM simulations. The substantial reduction of SST biases through flux adjustment leads to an improved representation of the summertime climatological large-scale flows, such as the monsoon ridge (Fig. 3) and the Caribbean low-level jet (not shown). A better representation of the annual cycle of SSTs over adjacent oceans also allows for more realistic rainfall distribution over AZWNM, consistent with what was shown by Liang et al. (2008). However, in FLOR-FA, AZWNM is drier than in observations. The reasons remain unclear, but we speculate that this may be due to either the lack of

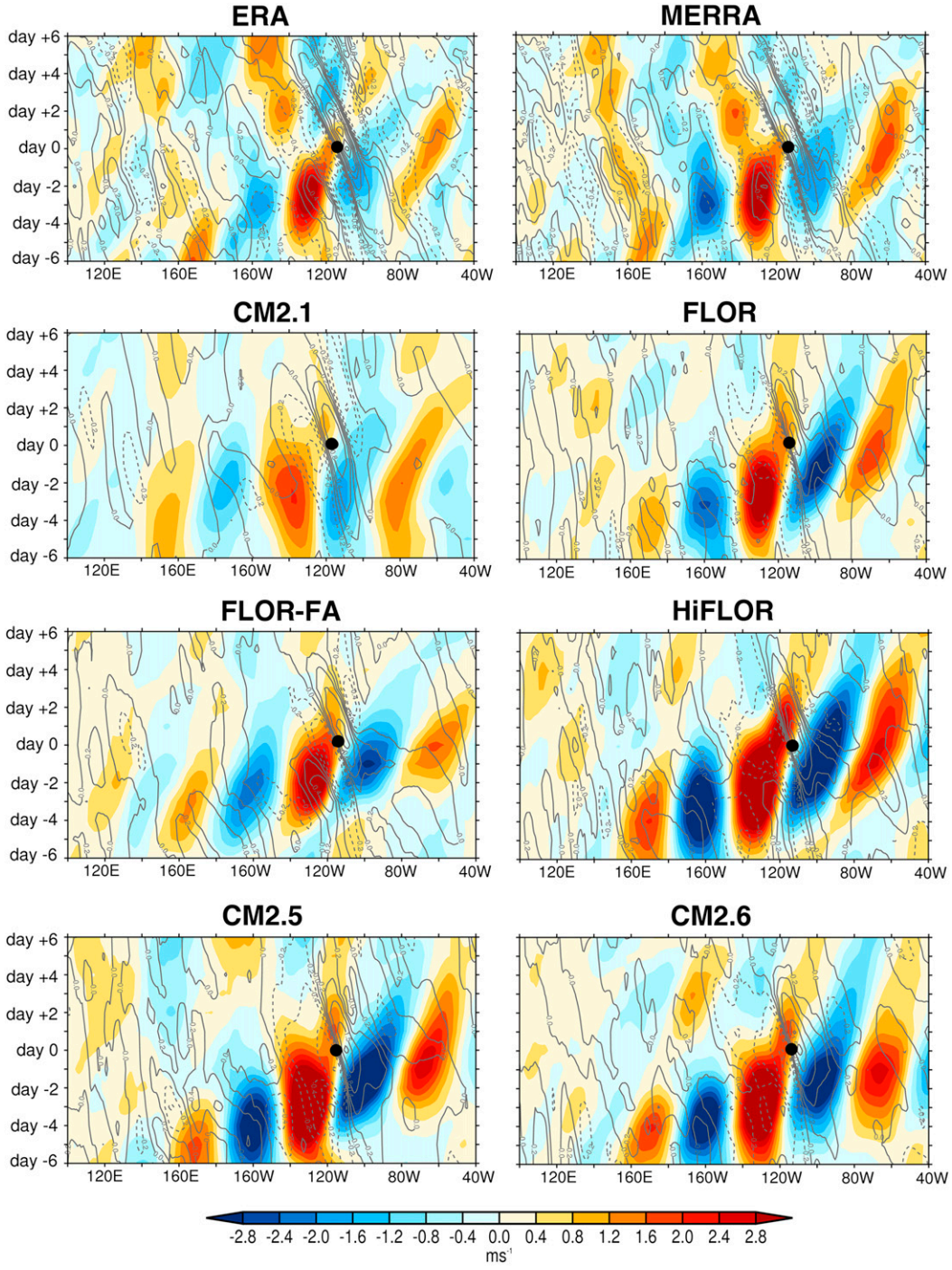

FIG. 12. Hovmöller longitude–time diagram of the 500-hPa lagged–regressed meridional wind anomalies (m s^{-1}) averaged between a narrow midlatitude (37°–43°N; color shading) and a tropical latitude (13°–17°N; contours) strip. The black dot denotes the longitude of the northern extremity of the GoC at day 0 (onset of the surge event).

ocean grid points (model grid points are land when they should be ocean as a result of gridding) in the northern part of the GoC (Schmitz and Mullen 1996; Berbery 2001) or, as discussed in the previous section, to reduced convective activity over the only partially resolved elevated terrain in AZWNM.

On a larger scale, SSTs in better agreement with observations result in a more realistic representation of

surge-related tropical easterly and extratropical Rossby waves (Fig. 12). While more research is needed to fully understand the impact of SST biases on large-scale tropical and extratropical waves affecting the NAM, the ameliorated wave representation might be linked to improvements in the simulation of the Caribbean low-level jet and the removal of large SST biases over the western Pacific. As easterly waves over the eastern Pacific are primarily driven by convective heating (Serra et al. 2008; Kiladis et al. 2009) and barotropic instability of the Caribbean low-level jet (Serra et al. 2010), it is plausible that these deficiencies primarily reflect deficiencies in how moist convection, as well as its interaction with larger-scale flows, is represented in climate models. Given the complexity of the interlinked factors, further research is needed in this direction.

6. Conclusions

In this study we examined the impact of horizontal atmosphere and ocean resolution on the simulation of Gulf of California (GoC) moisture surges within the North American monsoon in a suite of GFDL coupled global climate models with almost identical physical parameterizations. GoC surges are the main mechanism for lower-level moisture transport into the peripheral northern NAM region. This is the first time that GoC surges are investigated in detail by means of global coupled GCMs. We find the following:

1) As hypothesized, the increase of atmospheric horizontal resolution from 200 to 50 km dramatically improves simulations of near-surface features of GoC surges. In FLOR, FLOR-FA, CM2.5, CM2.6, and HiFLOR near-surface anomalous patterns associated with GoC surges, the monthly number of total and wet surge events per summer and surge contribution to summertime rainfall over AZWNM are overall satisfactorily simulated as compared to reanalyses.
2) The association between GoC surges and TEWs and/or TCs and RWTs, which tend to precede and provide the large-scale forcing of GoC surges, is overall well simulated; however, the TEW or TC teleconnection is overly weak relative to RWTs. While simulations of TEW features depend on and improve with increased horizontal resolution, RWTs appear to be less sensitive to it.
3) Flux adjustment in FLOR substantially reduces the positive SST biases over the Pacific Ocean. This is overall beneficial, as it leads to an improvement of the representation of the TEWs and RWTs preceding GoC surge events and of the seasonality of surge-related precipitation over the southwestern United States.

In this work we have focused on the mean climatological properties of GoC surges in coupled GCMs. Future studies will use nudged-SST simulations from the same models to assess the models' ability to reproduce NAM interannual variability over the southwestern United States (e.g., Small 2001; Castro et al. 2001).

One important implication emerging from this study is that the horizontal resolution of global climate models that are available in CMIP3 and CMIP5 and have been used to inform IPCC reports (resolutions $\geq$100 km with a mean of $\sim$200 km, comparable to the coarsest model in our analysis, CM2.1) does not allow for a faithful representation of the near-surface GoC surge flow and its contribution to NAM rainfall over the southwestern United States. Hence, future projections of hydroclimatic changes in the region based on CMIP3 and CMIP5 models must be reexamined with higher-resolution global models in order to assess whether the inability to represent GoC surges results in substantial errors in the projections. For example, the response of both mean and extreme rainfall to CO_2 doubling in the southwestern United States is different in FLOR and HiFLOR than in a lower-resolution version of the same model (van der Wiel et al. 2016). This suggests that representation of GoC surges may impact the rainfall response to CO_2 increase. Furthermore, although dynamical downscaling with regional models is a commonly used technique to extract added regional information from coarse GCMs, this study also suggests that a careful evaluation of large-scale controls of GoC moisture surges (i.e., TEWs and midlatitude westerly disturbances) is needed before dynamical downscaling is applied. For example, we would not recommend downscaling a GCM that severely underestimates TEW amplitude or frequency in the eastern Pacific since this would likely be reflected in weaker or less frequent GoC surges.

In conclusion, the high-resolution GFDL models perform satisfactorily in simulating the mean climatology of GoC surges and their dynamical and thermodynamical structure, paving the way for future studies of the NAM. Understanding the impact of global warming on the intensity and the intraseasonal variability of GoC surges, their large-scale dynamical forcing, and their contribution to the NAM precipitation over the southwestern United States is of vital importance for managing water resources in this region. Investigating how well mechanisms of NAM interannual variability related to tropical and North Pacific SSTs (El Niño–Southern Oscillation and the

Pacific decadal oscillation; e.g., Castro et al. 2001, 2007b) and soil moisture anomalies over the southern Rocky Mountains (e.g., because of the spring melt of above-normal snowpack) and in the NAM regions (e.g., Small 2001) are represented in this same suite of models is another important future task, given its particular relevance to seasonal predictability studies. Finally, these models can be used for targeted simulations with idealized boundary conditions in order to build a deeper mechanistic understanding of the main dynamical and thermodynamical shapers of the NAM.

Acknowledgments. S. P. was supported by the NOAA Climate and Global Change Postdoctoral Fellowship Program, administered by the University Corporation for Atmospheric Research, Boulder, Colorado. S. B. acknowledges support from the Davidow Discovery Fund. The authors are grateful to A. Rosati for the development of the CM2.5 and CM2.6 models, F. Zeng for producing the CM2.5 dataset, and K. Findell and three anonymous reviewers for constructive comments on a first version of this manuscript.

REFERENCES

Adams, D. K., and A. C. Comrie, 1997: The North American monsoon. *Bull. Amer. Meteor. Soc.*, **78**, 2197–2213, doi:10.1175/1520-0477(1997)078<2197:TNAM>2.0.CO;2.

Adams, J. L., and D. J. Stensrud, 2007: Impact of tropical easterly waves on the North American monsoon. *J. Climate*, **20**, 1219–1238, doi:10.1175/JCLI4071.1.

Aiyyer, A., and J. Molinari, 2008: MJO and tropical cyclogenesis in the Gulf of Mexico and eastern Pacific: Case study and idealized numerical modeling. *J. Atmos. Sci.*, **65**, 2691–2704, doi:10.1175/2007JAS2348.1.

Anderson, B. T., J. O. Roads, and S.-C. Chen, 2000: Large-scale forcing of summertime monsoon surges over the Gulf of California and the southwestern United States. *J. Geophys. Res.*, **105**, 24 455–24 467, doi:10.1029/2000JD900337.

Anderson, J. L., and Coauthors, 2004: The new GFDL global atmosphere and land model AM2–LM2: Evaluation with prescribed SST simulations. *J. Climate*, **17**, 4641–4673, doi:10.1175/1520-0442(2004)017<4089:IOALMO>2.0.CO;2.

Balling, R. C., 1987: Diurnal variations in Arizona monsoon precipitation frequencies. *Mon. Wea. Rev.*, **115**, 342–346, doi:10.1175/1520-0493(1987)115<0342:DVIAMP>2.0.CO;2.

Becker, A., P. Finger, A. Meyer-Christoffer, B. Rudolf, K. Schamm, U. Schneider, and M. Ziese, 2013: A description of the global land-surface precipitation data products of the Global Precipitation Climatology Centre with sample applications including centennial (trend) analysis from 1901–present. *Earth Syst. Sci. Data*, **5**, 71–99, doi:10.5194/essd-5-71-2013.

Beljaars, A. C. M., 1995: The parameterization of surface-fluxes in large-scale models under free convection. *Quart. J. Roy. Meteor. Soc.*, **121**, 255–270, doi:10.1002/qj.49712152203.

Berbery, E. H., 2001: Mesoscale moisture analysis of the North American monsoon. *J. Climate*, **14**, 121–137, doi:10.1175/1520-0442(2001)013<0121:MMAOTN>2.0.CO;2.

——, and M. S. Fox-Rabinovitz, 2003: Multiscale diagnosis of the North American monsoon system using a variable-resolution GCM. *J. Climate*, **16**, 1929–1947, doi:10.1175/1520-0442(2003)016<1929:MDOTNA>2.0.CO;2.

Berrisford, P., P. Kallberg, S. Kobayashi, D. Dee, S. Uppala, A. J. Simmons, P. Poli, and H. Sato, 2011a: Atmospheric conservation properties in ERA-Interim. *Quart. J. Roy. Meteor. Soc.*, **137**, 1381–1399, doi:10.1002/qj.864.

——, and Coauthors, 2011b: The ERA-Interim archive, version 2.0. ERA Rep. Series 1, 23 pp.

Bieda, S. W., C. L. Castro, S. L. Mullen, A. C. Comrie, and E. Pytlak, 2009: The relationship of transient upper-level troughs to variability of the North American monsoon system. *J. Climate*, **22**, 4213–4227, doi:10.1175/2009JCLI2487.1.

Bordoni, S., and B. Stevens, 2006: Principal component analysis of the summertime winds over the Gulf of California: A gulf surge index. *Mon. Wea. Rev.*, **134**, 3395–3414, doi:10.1175/MWR3253.1.

——, P. E. Ciesielski, R. H. Johnson, B. D. McNoldy, and B. Stevens, 2004: The low-level circulation of the North American monsoon as revealed by QuikSCAT. *Geophys. Res. Lett.*, **31**, L10109, doi:10.1029/2004GL020009.

Brenner, I. S., 1974: A surge of maritime tropical air—Gulf of California to the southwestern United States. *Mon. Wea. Rev.*, **102**, 375–389, doi:10.1175/1520-0493(1974)102<0375:ASOMTA>2.0.CO;2.

Castro, C. L., T. B. McKee, and R. A. Pielke Sr., 2001: The relationship of the North American monsoon to tropical and North Pacific sea surface temperatures as revealed by observational analyses. *J. Climate*, **14**, 4449–4473, doi:10.1175/1520-0442(2001)014<4449:TROTNA>2.0.CO;2.

——, R. A. Pielke Sr., and J. O. Adegoke, 2007a: Investigation of the summer climate of the contiguous United States and Mexico using the Regional Atmospheric Modeling System (RAMS). Part I: Model climatology (1950–2002). *J. Climate*, **20**, 3840–3865, doi:10.1175/JCLI4211.1.

——, S. D. Schubert, and P. J. Pegion, 2007b: Investigation of the summer climate of the contiguous United States and Mexico using the Regional Atmospheric Modeling System (RAMS). Part II: Model climate variability. *J. Climate*, **20**, 3866–3887, doi:10.1175/JCLI4212.1.

——, H.-I. Chang, F. Dominguez, C. Carrillo, J.-K. Schemm, and H.-M. H. Juang, 2012: Can a regional climate model improve the ability to forecast the North American monsoon? *J. Climate*, **25**, 8212–8237, doi:10.1175/JCLI-D-11-00441.1.

Cavazos, T., A. C. Comrie, and D. M. Liverman, 2002: Intraseasonal variability associated with wet monsoons in southeast Arizona. *J. Climate*, **15**, 2477–2490, doi:10.1175/1520-0442(2002)015<2477:IVAWWM>2.0.CO;2.

Ciancarelli, B., C. L. Castro, C. Woodhouse, F. Dominguez, H.-I. Chang, C. Carrillo, and D. Griffin, 2013: Dominant patterns of US warm season precipitation variability in a fine resolution observational record, with focus on the southwest. *Int. J. Climatol.*, **34**, 687–707, doi:10.1002/joc.3716.

Clough, S. A., M. J. Iacono, and J. Moncet, 1992: Line-by-line calculations of atmospheric fluxes and cooling rates: Application to water vapor. *J. Geophys. Res.*, **97**, 15 761–15 785, doi:10.1029/92JD01419.

Collier, J. C., and G. J. Zhang, 2007: Effects of increased horizontal resolution on simulation of the North American monsoon in the NCAR CAM3: An evaluation based on surface, satellite, and reanalysis data. *J. Climate*, **20**, 1843–1861, doi:10.1175/JCLI4099.1.

Cook, B. I., and R. Seager, 2013: The response of the North American monsoon to increased greenhouse gas forcing. *J. Geophys. Res. Atmos.*, **118**, 1690–1699, doi:10.1002/jgrd.50111.

Corbosiero, K. L., M. J. Dickinson, and L. F. Bosart, 2009: The contribution of eastern North Pacific tropical cyclones to the rainfall climatology of the southwest United States. *Mon. Wea. Rev.*, **137**, 2415–2435, doi:10.1175/2009MWR2768.1.

Dee, D. P., and Coauthors, 2011: The ERA-interim reanalysis: Configuration and performance of the data assimilation system. *Quart. J. Roy. Meteor. Soc.*, **137**, 553–597, doi:10.1002/qj.828.

Delworth, T. L., and F. Zeng, 2014: Regional rainfall decline in Australia attributed to anthropogenic greenhouse gases and ozone levels. *Nat. Geosci.*, **7**, 583–587, doi:10.1038/ngeo2201.

——, and Coauthors, 2006: GFDL's CM2 global coupled climate models. Part I: Formulation and simulation characteristics. *J. Climate*, **19**, 643–674, doi:10.1175/JCLI3629.1.

——, and Coauthors, 2012: Simulated climate and climate change in the GFDL CM2.5 high-resolution coupled climate model. *J. Climate*, **25**, 2755–2781, doi:10.1175/JCLI-D-11-00316.1.

——, F. Zeng, A. Rosati, G. A. Vecchi, and A. T. Wittenberg, 2015: A link between the hiatus in global warming and North American drought. *J. Climate*, **28**, 3834–3845, doi:10.1175/JCLI-D-14-00616.1.

Ding, Q., and B. Wang, 2005: Circumglobal teleconnection in the Northern Hemisphere summer. *J. Climate*, **18**, 3483–3505, doi:10.1175/JCLI3473.1.

Douglas, M. W., 1995: The summertime low-level jet over the Gulf of California. *Mon. Wea. Rev.*, **123**, 2334–2347, doi:10.1175/1520-0493(1995)123<2334:TSLLJO>2.0.CO;2.

——, and J. C. Leal, 2003: Summertime surges over the Gulf of California: Aspects of their climatology, mean structure, and evolution from radiosonde, NCEP reanalysis, and rainfall data. *Wea. Forecasting*, **18**, 55–74, doi:10.1175/1520-0434(2003)018<0055:SSOTGO>2.0.CO;2.

——, R. A. Maddox, K. Howard, and S. Reyes, 1993: The Mexican monsoon. *J. Climate*, **6**, 1665–1667, doi:10.1175/1520-0442(1993)006<1665:TMM>2.0.CO;2.

Duchon, C. E., 1979: Lanczos filtering in one and two dimensions. *J. Appl. Meteor.*, **18**, 1016–1022, doi:10.1175/1520-0450(1979)018<1016:LFIOAT>2.0.CO;2.

Erfani, E., and D. Mitchell, 2014: A partial mechanistic understanding of the North American monsoon. *J. Geophys. Res. Atmos.*, **119**, 13 096–13 115, doi:10.1002/2014JD022038.

Ferreira, D., and C. Frankignoul, 2005: The transient atmospheric response to midlatitude SST anomalies. *J. Climate*, **18**, 1049–1067, doi:10.1175/JCLI-3313.1.

Feser, F., B. Rockel, H. von Storch, J. Winterfeldt, and M. Zahn, 2011: Regional climate models add value to global model data: A review and selected examples. *Bull. Amer. Meteor. Soc.*, **92**, 1181–1192, doi:10.1175/2011BAMS3061.1.

Finch, Z. O., and R. H. Johnson, 2010: Observational analysis of an upper-level inverted trough during the 2004 North American monsoon experiment. *Mon. Wea. Rev.*, **138**, 3540–3555, doi:10.1175/2010MWR3369.1.

Freidenreich, S. M., and V. Ramaswamy, 1999: A new multiple-band solar radiative parameterization for general circulation models. *J. Geophys. Res.*, **104**, 31 389–31 409, doi:10.1029/1999JD900456.

Fu, Q., and K. N. Liou, 1993: Parameterization of the radiative properties of cirrus clouds. *J. Atmos. Sci.*, **50**, 2008–2025, doi:10.1175/1520-0469(1993)050<2008:POTRPO>2.0.CO;2.

Geil, K. L., Y. L. Serra, and X. Zeng, 2013: Assessment of CMIP5 model simulations of the North American monsoon system. *J. Climate*, **26**, 8787–8801, doi:10.1175/JCLI-D-13-00044.1.

Gilman, D. L., F. J. Fuglister, and J. M. Mitchell Jr., 1963: On the power spectrum of red noise. *J. Atmos. Sci.*, **20**, 182–184, doi:10.1175/1520-0469(1963)020<0182:OTPSON>2.0.CO;2.

Gnanadesikan, A., and Coauthors, 2006: GFDLs CM2 global coupled climate models. Part II: The baseline ocean simulation. *J. Climate*, **19**, 675–697, doi:10.1175/JCLI3630.1.

Gochis, D., C. Watts, J. Garatuza-Payan, and W. Shuttleworth, 2004: Analysis of 2002 and 2003 warm season precipitation from the North American monsoon experiment event rain gauge network. *Mon. Wea. Rev.*, **132**, 2938–2953, doi:10.1175/MWR2838.1.

Griffies, S. M., and Coauthors, 2005: Formulation of an ocean model for global climate simulations. *Ocean Sci.*, **1**, 45–79, doi:10.5194/os-1-45-2005.

Hales, J. E., 1972: Surges of maritime tropical air northward over the Gulf of California. *Mon. Wea. Rev.*, **100**, 298–306, doi:10.1175/1520-0493(1972)100<0298:SOMTAN>2.3.CO;2.

Hay, L. E., M. P. Clark, M. Pagowski, G. H. Leavesley, and W. J. Gutowski, 2006: One-way coupling of an atmospheric and a hydrologic model in Colorado. *J. Hydrometeor.*, **7**, 569–589, doi:10.1175/JHM512.1.

Higgins, R. W., and W. Shi, 2005: Relationships between Gulf of California moisture surges and tropical cyclones in the eastern Pacific basin. *J. Climate*, **18**, 4601–4620, doi:10.1175/JCLI3551.1.

——, Y. Yao, and X. L. Wang, 1997: Influence of the North American monsoon system on the U.S. summer precipitation regime. *J. Climate*, **10**, 298–306, doi:10.1175/1520-0442(1997)010<2600:IOTNAM>2.0.CO;2.

——, W. Shi, and C. Hain, 2004: Relationships between Gulf of California moisture surges and precipitation in the southwestern United States. *J. Climate*, **17**, 2983–2997, doi:10.1175/1520-0442(2004)017<2983:RBGOCM>2.0.CO;2.

Hu, H., and F. Dominguez, 2015: Evaluation of oceanic and terrestrial sources of moisture for the North American monsoon using numerical models and precipitation stable isotopes. *J. Hydrometeor.*, **16**, 19–35, doi:10.1175/JHM-D-14-0073.1.

Jia, L., and Coauthors, 2015: Improved seasonal prediction of temperature and precipitation over land in a high-resolution GFDL climate model. *J. Climate*, **28**, 2044–2062, doi:10.1175/JCLI-D-14-00112.1.

Jiang, X., and N. Lau, 2008: Intraseasonal teleconnection between North American and western North Pacific monsoons with 20-day time scale. *J. Climate*, **21**, 2664–2679, doi:10.1175/2007JCLI2024.1.

——, and D. E. Waliser, 2009: Two dominant subseasonal variability modes of the eastern Pacific ITCZ. *Geophys. Res. Lett.*, **36**, L04704, doi:10.1029/2008GL036820.

Kapnick, S. B., and T. L. Delworth, 2013: Controls of global snow under a changed climate. *J. Climate*, **26**, 5537–5562, doi:10.1175/JCLI-D-12-00528.1.

——, ——, M. Ashfaq, S. Malyshev, and P. C. D. Milly, 2014: Snowfall less sensitive to warming in Karakoram than in Himalayas due to a unique seasonal cycle. *Nat. Geosci.*, **7**, 834–840, doi:10.1038/ngeo2269.

Kikuchi, K., and B. Wang, 2009: Global perspective of the quasi-biweekly oscillation. *J. Climate*, **22**, 1340–1359, doi:10.1175/2008JCLI2368.1.

Kiladis, G. N., and E. A. Hall-McKim, 2004: Intraseasonal modulation of precipitation over the North American monsoon region. *Proc. 15th Symp. on Global Change and*

Climate Variations, Seattle, WA, Amer. Meteor. Soc., 11.4. [Available online at http://ams.confex.com/ams/pdfpapers/72428.pdf.]

——, M. C. Wheeler, P. T. Haertel, and K. H. Straub, 2009: Convectively coupled equatorial waves. *Rev. Geophys.*, **47**, RG2003, doi:10.1029/2008RG000266.

Kim, H., G. A. Vecchi, T. R. Knutson, W. G. Anderson, T. L. Delworth, A. Rosati, F. Zeng, and M. Zhao, 2014: Tropical cyclone simulation and response to CO_2 doubling in the GFDL CM2.5 high-resolution coupled climate model. *J. Climate*, **27**, 8034–8054, doi:10.1175/JCLI-D-13-00475.1.

King, T. S., and R. C. Balling, 1994: Diurnal variations in Arizona monsoon lightning data. *Mon. Wea. Rev.*, **122**, 1659–1664, doi:10.1175/1520-0493(1994)122<1659:DVIAML>2.0.CO;2.

Ladwig, W. C., and D. J. Stensrud, 2009: Relationship between tropical easterly waves and precipitation during the North American monsoon. *J. Climate*, **22**, 258–271, doi:10.1175/2008JCLI2241.1.

Lee, H.-C., and Coauthors, 2013: Impact of climate warming on upper layer of the Bering Sea. *Climate Dyn.*, **40**, 327–340, doi:10.1007/s00382-012-1301-8.

Liang, X., J. Zhu, K. E. Kunkel, M. Ting, and J. X. L. Wang, 2008: Do CGCMs simulate the North American monsoon precipitation seasonal–interannual variability? *J. Climate*, **21**, 4424–4448, doi:10.1175/2008JCLI2174.1.

Lin, J.-L., B. E. Mapes, K. M. Weickmann, G. N. Kiladis, S. D. Schubert, M. J. Suarez, J. T. Bacmeister, and M.-I. Lee, 2008: North American monsoon and convectively coupled equatorial waves simulated by IPCC AR4 coupled GCMs. *J. Climate*, **21**, 2919–2937, doi:10.1175/2007JCLI1815.1.

Lock, A. P., 2001: The numerical representation of entrainment in parameterizations of boundary layer turbulent mixing. *Mon. Wea. Rev.*, **129**, 1148–1163, doi:10.1175/1520-0493(2001)129<1148:TNROEI>2.0.CO;2.

Lorenz, D. J., and D. L. Hartmann, 2006: The effect of the MJO on the North American monsoon. *J. Climate*, **19**, 333–343, doi:10.1175/JCLI3684.1.

Lorenz, P., and D. Jacob, 2005: Influence of regional scale information on the global circulation: A two-way nesting climate simulation. *Geophys. Res. Lett.*, **32**, L18706, doi:10.1029/2005GL023351.

Maloney, E. D., and D. L. Hartmann, 2001: The Madden–Julian oscillation, barotropic dynamics, and North Pacific tropical cyclone formation. Part I: Observations. *J. Atmos. Sci.*, **58**, 2545–2558, doi:10.1175/1520-0469(2001)058<2545:TMJOBD>2.0.CO;2.

Meehl, G., and Coauthors, 2007: Global climate projections. *Climate Change 2007: The Physical Science Basis*, S. Solomon et al., Eds., Cambridge University Press, 747–846.

Mejia, J. F., M. W. Douglas, and P. J. Lamb, 2010: Aircraft observations of the 12–15 July 2004 moisture surge event during the North American monsoon experiment. *Mon. Wea. Rev.*, **138**, 3498–3513, doi:10.1175/2010MWR3228.1.

——, ——, and ——, 2015: Observational investigation of relationships between moisture surges and mesoscale- to large-scale convection during the North American monsoon. *Int. J. Climatol.*, **36**, 2555–2569, doi:10.1002/joc.4512.

Mesinger, F., Z. I. Janjić, S. Ničković, D. Gavrilov, and D. G. Deaven, 1988: The step-mountain coordinate: Model description and performance for cases of Alpine lee cyclogenesis and for a case of an Appalachian redevelopment. *Mon. Wea. Rev.*, **116**, 1493–1518, doi:10.1175/1520-0493(1988)116<1493:TSMCMD>2.0.CO;2.

Milly, P. C. D., and A. B. Shmakin, 2002: Global modeling of land water and energy balances. Part I: The land dynamics (LaD) model. *J. Hydrometeor.*, **3**, 283–299, doi:10.1175/1525-7541(2002)003<0283:GMOLWA>2.0.CO;2.

——, and Coauthors, 2014: An enhanced model of land water and energy for global hydrologic and Earth-system studies. *J. Hydrometeor.*, **15**, 1739–1761, doi:10.1175/JHM-D-13-0162.1.

Mo, K. C., 2000: Intraseasonal modulation of summer precipitation over North America. *Mon. Wea. Rev.*, **128**, 1490–1505, doi:10.1175/1520-0493(2000)128<1490:IMOSPO>2.0.CO;2.

——, J.-K. Schemm, H. M. H. Juang, R. W. Higgins, and Y. Song, 2005: Impact of model resolution on the prediction of summer precipitation over the United States and Mexico. *J. Climate*, **18**, 3910–3927, doi:10.1175/JCLI3513.1.

Molinari, J., D. Knight, M. Dickinson, D. Vollaro, and S. Skubis, 1997: Potential vorticity, easterly waves, and eastern Pacific tropical cyclogenesis. *Mon. Wea. Rev.*, **125**, 2699–2708, doi:10.1175/1520-0493(1997)125<2699:PVEWAE>2.0.CO;2.

Moorthi, S., and M. J. Suarez, 1992: Relaxed Arakawa–Schubert: A parameterization of moist convection for general circulation models. *Mon. Wea. Rev.*, **120**, 978–1002, doi:10.1175/1520-0493(1992)120<0978:RASAPO>2.0.CO;2.

Mullen, S. L., J. T. Schmitz, and N. O. Rennó, 1998: Intraseasonal variability of the summer monsoon over southeast Arizona. *Mon. Wea. Rev.*, **126**, 3016–3035, doi:10.1175/1520-0493(1998)126<3016:IVOTSM>2.0.CO;2.

Murakami, H., and Coauthors, 2015: Simulation and prediction of category 4 and 5 hurricanes in the high-resolution GFDL HiFLOR coupled climate model. *J. Climate*, **28**, 9058–9079, doi:10.1175/JCLI-D-15-0216.1.

Newman, A. J., and R. H. Johnson, 2012a: Mechanisms for precipitation enhancement in a North American monsoon upper-tropospheric trough. *J. Atmos. Sci.*, **69**, 1775–1792, doi:10.1175/JAS-D-11-0223.1.

——, and ——, 2012b: Simulation of a North American monsoon gulf surge event and comparison to observations. *Mon. Wea. Rev.*, **140**, 2534–2554, doi:10.1175/MWR-D-11-00223.1.

——, and ——, 2013: Dynamics of a simulated North American monsoon gulf surge event. *Mon. Wea. Rev.*, **141**, 3238–3253, doi:10.1175/MWR-D-12-00294.1.

Nolin, A. W., and E. A. Hall-McKim, 2006: Frequency modes of monsoon precipitation in Arizona and New Mexico. *Mon. Wea. Rev.*, **134**, 3774–3781, doi:10.1175/MWR3244.1.

Pascale, S., and S. Bordoni, 2016: Tropical and extratropical controls of Gulf of California surges and summertime precipitation over the southwestern United States. *Mon. Wea. Rev.*, **144**, 2695–2718, doi:10.1175/MWR-D-15-0429.1.

——, V. Lucarini, X. Feng, A. Porporato, and S. Hasson, 2016: Projected changes of rainfall seasonality and dry spells in a high greenhouse gas emissions scenario. *Climate Dyn.*, **46**, 1331–1350, doi:10.1007/s00382-015-2648-4.

Putman, W. M., and S. Lin, 2007: Finite-volume transport on various cubed-sphere grids. *J. Comput. Phys.*, **227**, 55–78, doi:10.1016/j.jcp.2007.07.022.

Pytlak, E., M. Goering, and A. Bennett, 2005: Upper-tropospheric troughs and their interaction with the North American monsoon. *19th Conf. on Hydrology*, San Diego, CA, Amer.

Meteor. Soc., JP2.3. [Available online at https://ams.confex.com/ams/Annual2005/techprogram/paper_85393.htm.]

Rienecker, M. M., and Coauthors, 2011: MERRA: NASA's Modern-Era Retrospective Analysis for Research and Applications. *J. Climate*, **24**, 3624–3648, doi:10.1175/JCLI-D-11-00015.1.

Ripa, P., and S. G. Marinone, 1989: Seasonal variability of temperature, salinity, velocity, vorticity and sea level in the central Gulf of California, as inferred from historical data. *Quart. J. Roy. Meteor. Soc.*, **115**, 887–913, doi:10.1002/qj.49711548807.

Rogers, P. J., and R. H. Johnson, 2007: Analysis of the 13–14 July gulf surge event during the 2004 North American monsoon experiment. *Mon. Wea. Rev.*, **135**, 3098–3117, doi:10.1175/MWR3450.1.

Rotstayn, L. D., 1997: A physically based scheme for the treatment of stratiform clouds and precipitation in large-scale models. I: Description and evaluation of microphysical processes. *Quart. J. Roy. Meteor. Soc.*, **123**, 1227–1282, doi:10.1002/qj.49712354106.

Schiffer, N. J., and S. W. Nesbitt, 2012: Flow, moisture, and thermodynamic variability associated with Gulf of California surges within the North American monsoon. *J. Climate*, **25**, 4220–4241, doi:10.1175/JCLI-D-11-00266.1.

Schmitz, J. T., and S. L. Mullen, 1996: Water vapor transport associated with the summertime North American monsoon as depicted by ECMWF analyses. *J. Climate*, **9**, 1621–1634, doi:10.1175/1520-0442(1996)009<1621:WVTAWT>2.0.CO;2.

Schneider, U., E. Becker, P. Finger, A. Meyer-Christoffer, M. Ziese, and B. Rudolf, 2014: GPCC's new land surface precipitation climatology based on quality-controlled in situ data and its role in quantifying the global water cycle. *Theor. Appl. Climatol.*, **115**, 15–40, doi:10.1007/s00704-013-0860-x.

Schwarzkopf, M. D., and V. Ramaswamy, 1999: Radiative effects of CH_4, N_2O, halocarbons and the foreign-broadened H_2O continuum: A GCM experiment. *J. Geophys. Res.*, **104**, 9467–9488, doi:10.1029/1999JD900003.

Seastrand, S., Y. Serra, C. Castro, and E. Ritchie, 2015: The dominant synoptic-scale modes of North American monsoon precipitation. *Int. J. Climatol.*, **35**, 2019–2032, doi:10.1002/joc.4104.

Serra, Y. L., G. N. Kiladis, and M. F. Cronin, 2008: Horizontal and vertical structure of easterly waves in the Pacific ITCZ. *J. Atmos. Sci.*, **65**, 1266–1284, doi:10.1175/2007JAS2341.1.

——, ——, and K. I. Hodges, 2010: Tracking and mean structure of easterly waves over the Intra-Americas Sea. *J. Climate*, **23**, 4823–4840, doi:10.1175/2010JCLI3223.1.

Slingo, A., 1989: A GCM parameterization for the shortwave radiative properties of water clouds. *J. Atmos. Sci.*, **46**, 1419–1427, doi:10.1175/1520-0469(1989)046<1419:AGPFTS>2.0.CO;2.

Small, E. E., 2001: The influence of soil moisture anomalies on variability of the North American monsoon system. *Geophys. Res. Lett.*, **28**, 139–142, doi:10.1029/2000GL011652.

Stensrud, D. J., R. L. Gall, and M. K. Nordquist, 1997: Surges over the Gulf of California during the Mexican monsoon. *Mon. Wea. Rev.*, **125**, 417–437, doi:10.1175/1520-0493(1997)125<0417:SOTGOC>2.0.CO;2.

Stern, W. F., and R. T. Pierrehumbert, 1988: The impact of an orographic gravity wave drag parameterization on extended range predictions with a GCM. Preprints, *Eighth Conf. on Numerical Weather Prediction*, Baltimore, MD, Amer. Meteor. Soc., 745–750.

Stratton, R. A., 1999: A high resolution AMIP integration using the Hadley Centre model HadAM2b. *Climate Dyn.*, **15**, 9–28, doi:10.1007/s003820050265.

Svoma, B. M., 2010: The influence of monsoonal gulf surges on precipitation and diurnal precipitation patterns in central Arizona. *Wea. Forecasting*, **25**, 281–289, doi:10.1175/2009WAF2222299.1.

Taylor, K. E., R. J. Stouffer, and G. A. Meehl, 2013: An overview of CMIP5 and the experiment design. *Bull. Amer. Meteor. Soc.*, **95**, 485–498, doi:10.1175/BAMS-D-11-00094.1.

Tiedtke, M., 1993: Representation of clouds in large-scale models. *Mon. Wea. Rev.*, **121**, 3040–3061, doi:10.1175/1520-0493(1993)121<3040:ROCILS>2.0.CO;2.

van der Wiel, K., and Coauthors, 2016: The resolution dependence of U.S. precipitation extremes in response to CO_2 forcing. *J. Climate*, doi:10.1175/JCLI-D-16-0307.1, in press.

Vecchi, G. A., and Coauthors, 2013: Multi-year predictions of North Atlantic hurricane frequency: Promise and limitations. *J. Climate*, **26**, 5337–5357, doi:10.1175/JCLI-D-12-00464.1.

——, and Coauthors, 2014: On the seasonal forecasting of regional tropical cyclone activity. *J. Climate*, **27**, 7994–8016, doi:10.1175/JCLI-D-14-00158.1.

Watt-Meyer, O., and P. J. Kushner, 2015: Decomposition of atmospheric disturbances into standing and travelling components, with applications to Northern Hemisphere planetary waves and stratosphere–troposphere coupling. *J. Atmos. Sci.*, **72**, 787–802, doi:10.1175/JAS-D-14-0214.1.

Wittenberg, A. T., A. Rosati, N. Lau, and J. J. Ploshay, 2006: GFDL's CM2 global coupled climate models. Part III: Tropical Pacific climate and ENSO. *J. Climate*, **19**, 698–722, doi:10.1175/JCLI3631.1.

——, ——, T. L. Delworth, G. A. Vecchi, and F. Zeng, 2014: ENSO modulation: Is it decadally predictable? *J. Climate*, **27**, 2667–2681, doi:10.1175/JCLI-D-13-00577.1.

Wood, K. M., and E. A. Ritchie, 2013: An updated climatology of tropical cyclone impacts on the southwestern United States. *Mon. Wea. Rev.*, **141**, 4322–4336, doi:10.1175/MWR-D-13-00078.1.

Wu, M.-L. C., S. D. Schubert, M. J. Suarez, and N. E. Huang, 2009: An analysis of moisture fluxes into the Gulf of California. *J. Climate*, **22**, 2216–2239, doi:10.1175/2008JCLI2525.1.

Yang, X., and Coauthors, 2013: A predictable AMO-like pattern in the GFDL fully coupled ensemble initialization and decadal forecasting system. *J. Climate*, **26**, 650–661, doi:10.1175/JCLI-D-12-00231.1.

Zehnder, J. A., 2004: Dynamic mechanisms of the gulf surge. *J. Geophys. Res.*, **109**, D10107, doi:10.1029/2004JD004616.